A validated patient–specific FSI model for vascular access in haemodialysis

AM de Villiers [1,2] · **AT McBride** [1,3] · **BD Reddy** [1] · **T Franz** [4] · **BS Spottiswoode** [5]

Received: date / Accepted: date

Abstract The flow rate inside arteriovenous fistulas is many times higher than physiological flow and is accompanied by high wall shear stress resulting in low patency rates. A fluid–structure interaction finite element model is developed to analyze the blood flow and vessel mechanics to elucidate the mechanisms that can lead to failure. The simulations are validated against flow measurements obtained from magnetic resonance imaging data.

Keywords fluid–structure interaction · fistula · blood flow · finite elements · pre-stress

1 Introduction

Haemodialysis is the most common treatment for patients with end stage renal disease (ESRD). During haemodialysis, blood is circulated through a filter that removes fluid and waste products, after which it is returned to the body. An arteriovenous shunt is formed to achieve the high flow rates (at least 350 ml/min (Malik et al, 2009)) necessary to make haemodialysis possible. The preferred form of vascular access is the arteriovenous fistula (AVF), a connection between the artery and vein (Allon and Robbin, 2002). Fistulas are created at the most distal site possible, usually between the radial artery and the cephalic vein. When these fistulas are blocked, access sites are created proximally to the blocked site (Fig. 1). In these proximal access sites, where the brachial artery is connected to either the basilic vein or the cephalic vein, flow rates can be up to 30 times higher than normal flow in the brachial artery (Huberts et al, 2012).

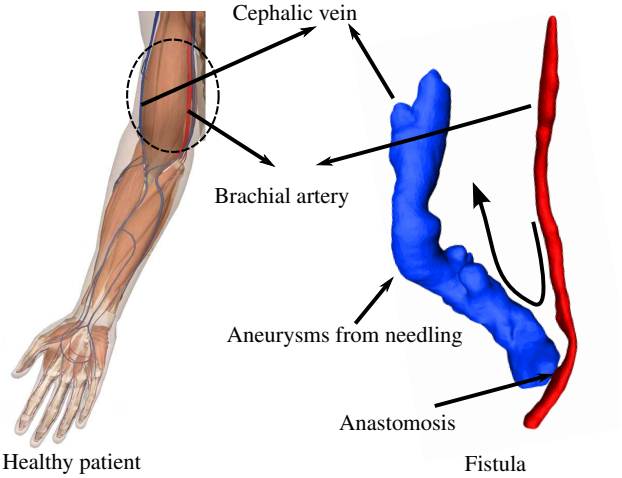

Fig. 1 Anatomy of a healthy patient showing the site where a brachiocephalic fistula would be created (left) and an MRI scan of a patient–specific fistula (right)

The flow in the vein changes significantly after vascular access creation, making the haemodynamics of the AVF unique in the vasculature; the pressure increases from about 20 mmHg to between 60 and 120 mmHg, flow increases and changes from steady to pulsatile, and the wall shear stress (WSS) is significantly higher. The combination of pulsatile flow and high WSS creates a high oscillatory wall shear

[1] Centre for Research in Computational and Applied Mechanics
University of Cape Town

[2] Division of Applied Mathematics
Stellenbosch University
Tel.: +27 21 808-4215
E-mail: andiedevilliers@sun.ac.za

[3] School of Engineering
University of Glasgow

[4] Division of Biomedical Engineering
University of Cape Town

[5] Siemens Medical Solutions USA, Inc.

stress and large spatial and temporal gradients of the WSS. To complicate matters further, pseudo–aneurysms may form as a result of the frequent needling necessary for dialysis.

It is not surprising that the patency rates of AFVs are low. The primary pathology of vascular access is thrombosis. Thrombosis is caused by progressive stenosis (abnormal narrowing in the blood vessel) which is primarily found at the heel and toe of the anastomosis and also in the vein downstream of the junction where flow is turbulent (Haruguchi and Teraoka, 2003). Intimal hyperplasia (IH) is the underlying mechanism of stenosis. There is no consensus on the pathogenesis of IH. Although most computational studies link low or oscillating shear to the development of IH, a number of studies found that high shear and high spatial and temporal WSS gradients are associated with the onset of IH (Cunnane et al, 2017).

There have been various approaches aimed at improving the computational modelling of vascular access. Huberts et al (2012) developed a 1D network model to predict the post–operative flow following vascular access surgery. To study flow features such as recirculation, stagnation and separation in more detail, computational fluid dynamics (CFD) simulations have been used (Lee et al, 2007; Niemann et al, 2010; Van Canneyt et al, 2010). Most CFD studies approximated blood as a Newtonian fluid, but the effects of shear thinning have been investigated (Ene-Iordache and Remuzzi, 2012; Ryou et al, 2013). CFD models have been used to study different configurations of AVFs (Ene-Iordache and Remuzzi, 2012), the influence that the curvature of the fistula or graft has on flow patterns (Boghosian et al, 2014; Iori et al, 2015) and the transition from laminar to turbulent flow (Bozzetto et al, 2016). Validation of these models remains a difficult task; some researchers compare their results to data from in vitro studies (Browne et al, 2014) or in vivo flow obtained by Doppler anemometry (Hammes et al, 2016), two–dimensional venograms (Boghosian et al, 2014) or particle image velocimetry (Kharboutly et al, 2010).

Compared to the abundant CFD studies of arteriovenous fistulas, fluid–structure interaction (FSI) studies are rare. The FSI model can however provide insights into the onset of IH by including stresses in vessel walls and pressure wave propagation. Ngoepe et al (2011) developed a coupled numerical tool to study both haemodynamics of blood and mechanics of the vessels in a simplified artery–graft–vein configuration. Decorato et al (2011) found that WSS is overestimated by 10-13% with the use of rigid wall simulation in a patient–specific AVF. McGah et al (2014) compared the WSS between rigid wall and FSI simulations. These studies used a partitioned approach for the interaction. There appear to be no studies in the literature that use a monolithic approach in FSI investigations of arteriovenous shunts. The monolithic approach circumvents the "added-mass" effect (Causin et al, 2005), an instability that is present when a staggered approach is used for a long slender domain or when the fluid and solid densities are of the same order.

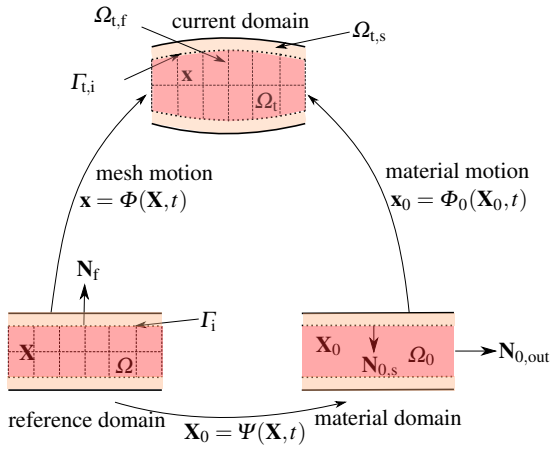

Fig. 2 The various domains and motions that comprise the ALE model

This work integrates state–of–the–art modeling into a robust numerical framework. The computational model accounts for both blood flow and vessel wall mechanics as well as physically-motivated boundary conditions and perivascular support. A monolithic FSI model to simulate an arteriovenous fistula is detailed. The simulation is verified against flow results processed from magnetic resonance imaging (MRI) data. The outline of the presentation is as follows. Section 2 presents the governing equations in the strong and weak forms and describes the boundary conditions. Section 3 describes the numerical implementation, including the finite element discretization and the solution of the block structured linear equations. Section 4 presents results of the simulation and the validation against MRI data. In the final section the results are discussed.

2 Biomechanical model

The Arbitrary Lagrangian–Eulerian (ALE) description combines the ability of the Lagrangian description to easily track moving interfaces, with the ability of the Eulerian description to handle large distortions (Hughes et al, 1981). In order to present the governing equations in the ALE framework, various domains are defined (**Fig. 2**). The reference domain is denoted by Ω, and the material domain by Ω_0. The current domain at time t is denoted by Ω_t. At $t = 0$, the position vector $\mathbf{X}$ denotes the referential positions of particles in the reference domain Ω, and the various domains (material, reference and current) coincide. The position vector is denoted by $\mathbf{X}_0$ in the material domain and $\mathbf{x}$ in the current domain. The boundary of the reference domain is denoted by $\partial\Omega = \Gamma = \Gamma_D \cup \Gamma_N$, where Γ_D denotes the Dirichlet part

of the boundary and Γ_{N} denotes the Neumann part. Γ_D and Γ_N are nonoverlapping. Similarly, the boundaries of the material and current domains are denoted respectively by Γ_0 and Γ_{t}.

We differentiate between the subdomain associated with the fluid, denoted by subscript f, and the subdomain associated with the structure, denoted by subscript s. The interface between the two subdomains is denoted by $\Gamma_{\mathrm{i}} = \partial\Omega_{\mathrm{s}} \cap \partial\Omega_{\mathrm{f}}$ in the reference domain. Various maps are defined to describe the motion between the various domains. The material domain Ω_0 is mapped from the reference domain Ω by $\mathbf{X}_0 = \Psi(\mathbf{X},t)$. The mesh motion is mapped from the reference domain to the current domain by $\mathbf{x} = \Phi(\mathbf{X},t)$. The motion of the material is mapped from the material domain to the spatial domain by the material map $\mathbf{x} = \Phi_0(\mathbf{X}_0,t)$. The displacement $\mathbf{u}$ relates $\mathbf{X}_0$ in the material domain to the position $\mathbf{x}$ in the current configuration at time t, and is defined by

$$\mathbf{u}\big(\mathbf{X}_0,t\big) = \mathbf{x} - \mathbf{X}_0 = \Phi_0(\mathbf{X}_0,t) - \mathbf{X}_0.$$

The deformation gradient $\mathbf{F}$ is defined by

$$\mathbf{F}\big(\mathbf{X}_0,t\big) = \frac{\partial \Phi_0\big(\mathbf{X}_0,t\big)}{\partial \mathbf{X}_0}.$$

$\mathbf{F}$ characterizes the deformation in the neighbourhood of a material point $\mathbf{X}_0$. The right Cauchy–Green tensor is defined by $\mathbf{C} = \mathbf{F}^T\mathbf{F}$. The volume change is defined by $J = \det\mathbf{F}$.

In an ALE framework, fields are usually expressed as functions of the reference coordinates $\mathbf{X}$ and time t. The material time derivative of a arbitrary referential field f is given by

$$\begin{aligned}\dot{f}\big(\mathbf{X},t\big) &= \frac{\partial f\big(\mathbf{X},t\big)}{\partial t} + \frac{\partial f\big(\mathbf{X},t\big)}{\partial \mathbf{X}} \cdot \frac{\partial \Psi^{-1}\big(\mathbf{X}_0,t\big)}{\partial t}\bigg|_{\mathbf{X}_0=\Psi^{-1}\left(\mathbf{X},t\right)} \\ &= \frac{\partial f}{\partial t} + \mathrm{Grad} f \cdot \frac{\partial \mathbf{X}}{\partial \mathrm{t}} \\ &= \frac{\partial f}{\partial t} + \nabla f \cdot \left(\mathrm{Grad}\,\mathbf{x}\frac{\partial \mathbf{X}}{\partial \mathrm{t}}\right). \end{aligned} \tag{1}$$

Grad refers to the gradient in the reference domain and ∇f to the gradient in the current domain.

In order to develop a relationship between the velocity and the mesh velocity, the expression for material motion $\mathbf{x} = \Phi_0(\mathbf{X}_0,t)$ can be rewritten as a composition of functions as $\mathbf{x} = \Phi_0(\mathbf{X}_0,t) = \Phi(\Psi^{-1}\big(\mathbf{X}_0,t\big),t)$. From this and the chain rule, the mesh velocity can be expressed as

$$\begin{aligned}\mathbf{v} = \mathbf{V}_0 &= \dot{\Phi}_0\big(\mathbf{X}_0,t\big) = \dot{\Phi}\big(\Psi^{-1}\big(\mathbf{X}_0,t\big),t\big) \\ &= \frac{\partial \Phi\big(\mathbf{X},t\big)}{\partial t} + \frac{\partial \Phi\big(\mathbf{X},t\big)}{\partial \mathbf{X}}\,\frac{\partial \Psi^{-1}\big(\mathbf{X}_0,t\big)}{\partial t}\bigg|_{\mathbf{X}_0=\Psi^{-1}\left(\mathbf{X},t\right)} \\ &= \mathbf{V} + \mathrm{Grad}\,\mathbf{x}\frac{\partial \mathbf{X}}{\partial \mathrm{t}} \\ &= \mathbf{V} + \mathbf{c}. \end{aligned}$$

The convective velocity $\mathbf{c}$ is defined as the difference between the material and mesh velocities.

The material time derivative in (1) can therefore be rewritten as

$$\dot{f}\big(\mathbf{X},t\big) = \frac{\partial f}{\partial t} + \mathbf{c}\cdot\nabla f. \tag{2}$$

2.1 Governing equations

2.1.1 Governing equations for the fluid in ALE framework

Using (2) for the time derivative of the velocity, the Navier–Stokes equations in the current fluid configuration, $\Omega_{\mathrm{t,f}}$, are given by

$$\begin{aligned}\rho_{\mathrm{f}}\left(\frac{\partial \mathbf{v}}{\partial t} + \mathbf{c}\cdot\nabla\mathbf{v}\right) - \mathrm{div}\sigma_{\mathrm{f}} = \mathbf{0} \quad &\text{in} \quad \Omega_{\mathrm{t,f}}, \\ \mathrm{div}\mathbf{v} = 0 \quad &\text{in} \quad \Omega_{\mathrm{t,f}}, \\ \mathbf{v} = \mathbf{v}^{\mathrm{D}} \quad &\text{on} \quad \Gamma_{\mathrm{t,f,D}}, \\ \sigma\mathbf{n} = \mathbf{g}_{\mathrm{f}} \quad &\text{on} \quad \Gamma_{\mathrm{t,f,N}}. \end{aligned} \tag{3}$$

Here $\mathbf{g}_{\mathrm{f}}$ and $\mathbf{v}^{\mathrm{D}}$ are the traction prescribed on the Neumann boundary and the velocity prescribed on the Dirichlet boundary, respectively. The Cauchy stress tensor is defined by

$$\sigma_{\mathrm{f}} = -p_{\mathrm{f}}\mathbf{I} + \mu_{\mathrm{f}}(\nabla\mathbf{v} + \nabla\mathbf{v}^T),$$

where $\mathbf{v}$ and and p denote the fluid velocity and pressure, respectively. For a Newtonian fluid, as assumed here, the effective viscosity μ_{f} is constant.

2.1.2 Governing equations for solid in the material configuration

The equation of motion and boundary conditions in the material configuration are given by

$$\begin{aligned}\rho_{\mathrm{s}}\frac{\partial \mathbf{v}}{\partial t} - \mathrm{Div}\mathbf{P} = \mathbf{0} \ \text{ in } \ \Omega_{0,\mathrm{s}}, \\ \mathbf{u} = \mathbf{u}^{\mathrm{D}} \ \text{ on } \ \Gamma_{0,\mathrm{s,D}}, \quad \mathbf{PN} = \mathbf{g}_{\mathrm{s}} \ \text{ on } \ \Gamma_{0,\mathrm{s,N}}. \end{aligned} \tag{4}$$

Here $\mathbf{P}$ is the first Piola–Kirchhoff stress tensor, $\mathbf{g}_\mathrm{s}$ the traction prescribed at the Neumann boundary, $\mathbf{u}^\mathrm{D}$ the displacement prescribed at the Dirichlet boundary and $\mathbf{N}$ is the outward unit normal in the material configuration. For a hyperelastic material

$$\mathbf{P} = \frac{\partial \psi(\mathbf{F})}{\partial \mathbf{F}}, \tag{5}$$

where ψ is the free energy density and is given here by a widely used model developed by Holzapfel et al (2000) and extended in Gasser et al (2006) to include dispersion of the fibres. The model represents the vessel as a matrix material in which two families of fibres are embedded. The free energy is split additively into a part associated with the ground matrix ψ_g and a part associated with the anisotropic deformation ψ_fib, that is

$$\psi = \psi_\mathrm{g}(I_1, I_2, I_3) + \psi_\mathrm{fib}(I_4, I_5, I_6, I_7, I_8, I_9). \tag{6}$$

Here I_i denotes an invariant of $\mathbf{C}$, with I_1, I_2, I_3 associated with the ground matrix and I_4, I_5, I_6, I_7, I_8 associated with the two directions of the fibres embedded in the ground matrix, that is

$$\begin{aligned} I_1(\mathbf{C}) = \mathrm{tr}\mathbf{C}, \quad I_2(\mathbf{C}) = \frac{1}{2}[(\mathrm{tr}\mathbf{C})^2 - \mathrm{tr}\mathbf{C}^2], \quad \mathrm{I}_3(\mathbf{C}) = \mathrm{det}\mathbf{C}, \\ I_4(\mathbf{C}, \mathbf{A_1}) = \mathbf{C} : \mathbf{A_1}, \quad I_5(\mathbf{C}, \mathbf{A_1}) = \mathbf{C}^2 : \mathbf{A_1}, \\ I_6(\mathbf{C}, \mathbf{A_2}) = \mathbf{C} : \mathbf{A_2}, \quad I_7(\mathbf{C}, \mathbf{A_2}) = \mathbf{C}^2 : \mathbf{A_2}, \\ I_8(\mathbf{C}, \mathbf{A_1}, \mathbf{A_2}) = (\mathbf{a}_{0,1} \cdot \mathbf{a}_{0,2})\mathbf{a}_{0,1} \cdot \mathbf{C}\mathbf{a}_{0,2}, \\ I_9(\mathbf{A_1}, \mathbf{A_2}) = (\mathbf{a}_{0,1} \cdot \mathbf{a}_{0,2})^2. \end{aligned} \tag{7}$$

The unit vectors $\mathbf{a}_{0,i}(\mathbf{X}_0)$, $i = 1,2$, define the directions of the fibres at point $\mathbf{X}_0$ and $\mathbf{A}_i = \mathbf{a}_\mathrm{i} \otimes \mathbf{a}_\mathrm{i}$. To reduce the number of material parameters, note that I_9 is a constant and I_4 and I_6 are the squares of the stretches in the directions of the fibres, hence $\Psi_\mathrm{fib} = \Psi_\mathrm{fib}(I_4, I_6)$. The strong stiffening effect of the arteries motivates the use of an exponential function for Ψ_fib. The free-energy associated with the fibres is given by

$$\psi_\mathrm{fib} = \frac{k_1}{2k_2} \sum_{i=4,6} \left(\exp\left(k_2 \left(\kappa I_1 + (1 - 3\kappa) I_i - 1 \right)^2 \right) - 1 \right), \tag{8}$$

where k_1 is a stress–like parameter, k_2 is a non–dimensional number, and κ is a parameter associated with the dispersion of the fibres ($\kappa = 0$ implies no dispersion).

2.1.3 Harmonic mesh motion

For moderate deformations (as in the vessel walls), the mesh motion can be described with an auxillary Laplace equation and is termed a harmonic mesh motion. The harmonic equation and boundary conditions in the reference configuration are:

$$\begin{aligned} -\mathrm{Div}\mathbf{P}_\mathrm{m} = \mathbf{0} \quad \text{in} \quad \Omega_\mathrm{f}, \\ \mathbf{u}_\mathrm{f} = \mathbf{u}_\mathrm{s} \quad \text{on} \quad \Gamma_\mathrm{i}, \quad \mathbf{u}_\mathrm{f} = \mathbf{0} \quad \text{on} \quad \partial\Omega \cap \Gamma_\mathrm{i}, \end{aligned} \tag{9}$$

where $\mathbf{P}_\mathrm{m} = \alpha \mathrm{Grad}\,\mathbf{u}$. The diffusion parameter α ensures good fluid mesh quality and is chosen as $\alpha(\mathbf{x}) = (J-1)^2$. This choice ensures that as an element distorts, it becomes more stiff and increasingly resistant to further distortion.

2.1.4 Coupling conditions

The interface conditions between the fluid domain Ω_f and the solid domain Ω_s on the coupling interface Γ_i are given by

$$\mathbf{v}_\mathrm{f} = \frac{\partial \mathbf{u}_\mathrm{f}}{\partial t} = \mathbf{v}_\mathrm{s} \quad \text{on} \quad \Gamma_\mathrm{i}, \quad \mathbf{P}_\mathrm{s}\mathbf{N}_\mathrm{s} + J\sigma\mathbf{F}^{-T}\mathbf{n}_\mathrm{f} = \mathbf{0} \quad \text{on} \quad \Gamma_\mathrm{i}. \tag{10}$$

2.2 Weak form of governing equations

As the equations will be solved monolithically using the finite element method, the weak form of the equations are written in the reference configuration. Standard notation for Lebesgue and Sobolev spaces is used. The space of square-integrable functions which satisfy the homogeneous Dirichlet boundary conditions are defined by $L^2_D(\mathbf{X}) = \left\{ \mathbf{u} \in \left[L^2(\mathbf{X}) \right]^3 : \mathbf{u} = \mathbf{0} \text{ on } \Gamma_\mathrm{D} \right\}$. The space of functions which, together with their first derivatives, are square-integrable, and which satisfy the homogeneous Dirichlet boundary conditions are defined by $H^1_D(X) = \left\{ \mathbf{u} \in \left[L^2_D(\mathbf{X}) \right]^3 \text{ and } \frac{\partial \mathrm{u_i}}{\partial \mathrm{X_j}} \in \left[\mathrm{L}^2_\mathrm{D}(\mathbf{X}) \right] : \mathbf{u} = \mathbf{0} \text{ on } \Gamma_\mathrm{D} \right\}$.

2.2.1 Weak form of the Navier-Stokes equations

Multiplication of (3) by test functions $\delta\mathbf{v}$ and δp respectively, integration over the domain, integration by parts and a pull back to the reference configuration gives

$$\begin{aligned} \int_{\Omega_\mathrm{f}} \left(\delta\mathbf{v} \cdot J\rho_\mathrm{f} \frac{\partial \mathbf{v}}{\partial t} \right) \mathrm{dV} + \int_{\Omega_\mathrm{f}} \left(\delta\mathbf{v} \cdot \mathrm{J}\rho_\mathrm{f} \mathrm{Grad}\,\mathbf{v}\mathbf{F}^{-1} \left(\mathbf{v} - \frac{\partial \mathbf{u}}{\partial \mathrm{t}} \right) \right) \mathrm{dV} \\ + \int_{\Omega_\mathrm{f}} \left(\nabla \delta\mathbf{v} : J\sigma_\mathrm{f}\mathbf{F}^{-T} \right) \mathrm{dV} - \int_{\Gamma_\mathrm{f}} \left(\delta\mathbf{v} \cdot \mathbf{g}_\mathrm{f} \right) \mathrm{dS} = 0 \quad \forall \delta\mathbf{v} \in \mathrm{H}^1_\mathrm{D}, \\ \int_{\Omega_\mathrm{f}} \left(\delta p \cdot \mathrm{Div}\left(J\mathbf{F}^{-1}\mathbf{v} \right) \right) \mathrm{dV} = 0 \quad \forall \delta \mathrm{p} \in \mathrm{L}^2_\mathrm{D}. \end{aligned} \tag{11}$$

σ_f can be expressed in terms of the material gradient as

$$\sigma_\mathrm{f} = -p_\mathrm{f}\mathbf{I} + \rho_\mathrm{f}\nu_\mathrm{f} \left(\mathrm{Grad}\,\mathbf{v}\mathbf{F}^{-1} + \mathbf{F}^{-\mathrm{T}} \left(\mathrm{Grad}\,\mathbf{v} \right)^\mathrm{T} \right), \tag{12}$$

where ν_f is the kinematic viscosity.

2.2.2 Weak form of fibre-reinforced solid equations

Incompressible materials Incompressible materials are characterized by the constraint

$$J = 1 \text{ or } \operatorname{div}\mathbf{v} = 0. \tag{13}$$

To eliminate locking phenomena, a mixed finite element formulation is used wherein a Lagrange–multiplier is used to enforce the incompressibility constraint (Holzapfel, 2002). For this formulation, it is standard to employ a decoupled representation of the free–energy density:

$$\psi(\mathbf{C}) = \psi_{\text{vol}}(J) + \psi_{\text{iso}}(\bar{\mathbf{C}}). \tag{14}$$

The isochoric part of the free–energy function Ψ_{iso} is a function of the modified right Cauchy–Green tensor $\bar{\mathbf{C}}(\mathbf{u}) = J^{-2/3}\mathbf{C}$. The internal energy functional Ψ_{int} is also formulated in the decoupled representation:

$$\Psi_{\text{int}}(\mathbf{u}, p) = \int_{\Omega_0} \left[p\big(J(\mathbf{u}) - 1\big) + \Psi_{\text{iso}}(\bar{\mathbf{C}}(\mathbf{u}))\right] \mathrm{dV}, \tag{15}$$

where p is the Lagrange–multiplier.

The stationarity conditions following from the principle of minimum potential energy are given by

$$\begin{aligned} D_{\delta\mathbf{u}}\Psi(\mathbf{u}, p) &= \int_{\Omega_0} \big(Jp\mathbf{F}^{-1} : \operatorname{Grad}\delta\mathbf{u} + \mathbf{P} : \operatorname{Grad}\delta\mathbf{u}\big)\mathrm{dV} = 0, \\ D_{\delta p}\Psi(\mathbf{u}, p) &= \int_{\Omega_0} (J(\mathbf{u}) - 1)\delta p \mathrm{dV} = 0. \end{aligned} \tag{16}$$

Constitutive model for fibre-reinforced material The first Piola–Kirchoff stress $\mathbf{P}$ is now derived for the vessel wall: an incompressible fibre–reinforced material. The isochoric part of $\psi(\mathbf{C})$ in (14) can be split into a part associated with the ground matrix and a part associated with the anisotropic deformation:

$$\begin{aligned} \psi_{\text{iso}} &= \psi_{\text{g}} + \psi_{\text{fib}} \\ &= \frac{\mu}{2}(\bar{I}_1 - 3) + \sum_{i=4,6} \psi_{\text{fib}}(\bar{I}_i), \end{aligned} \tag{17}$$

where μ is the shear modulus. The invariants for the isochoric part are (cf. 7)

$$\begin{aligned} \bar{I}_1 &= \bar{\mathbf{C}} : \mathbf{I} = J^{-\frac{2}{3}}\mathbf{C} : \mathbf{I} = J^{-\frac{2}{3}} I_1, \\ \bar{I}_4 &= \bar{\mathbf{C}} : \mathbf{A}_1 = J^{-\frac{2}{3}}\mathbf{C} : \mathbf{A}_1 = J^{-\frac{2}{3}} I_4, \\ \bar{I}_6 &= \bar{\mathbf{C}} : \mathbf{A}_1 = J^{-\frac{2}{3}}\mathbf{C} : \mathbf{A}_2 = J^{-\frac{2}{3}} I_6. \end{aligned} \tag{18}$$

The second Piola–Kirchhoff stress tensor $\mathbf{S}$ is given by $\mathbf{P} = \mathbf{F}\mathbf{S}$ where

$$\mathbf{S} = 2\frac{\partial \psi}{\partial \mathbf{C}}.$$

$\mathbf{S}$ is written in the decoupled representation as

$$\mathbf{S} = \mathbf{S}_{\text{g}} + \mathbf{S}_{\text{fib}} = 2\left(\frac{\partial \psi_{\text{g}}(\bar{\mathbf{C}})}{\partial \mathbf{C}} + \frac{\partial \psi_{\text{fib}}(\bar{\mathbf{C}})}{\partial \mathbf{C}} \right). \tag{19}$$

The second and first Piola–Kirchhoff stresses associated with the ground substance are given by

$$\begin{aligned} \mathbf{S}_{\text{g}} &= 2\frac{\partial \psi_{\text{g}}(\bar{\mathbf{C}})}{\partial \mathbf{C}} \\ &= 2\frac{\partial \psi_{\text{g}}(\bar{\mathbf{C}})}{\partial \bar{\mathbf{C}}} \frac{(\partial \bar{\mathbf{C}})}{\partial \mathbf{C}} \\ &= \mu J^{-\frac{2}{3}}\mathbf{I} - \big(\frac{\mu J^{-\frac{2}{3}} I_1}{3}\big)\mathbf{C}^{-1}, \end{aligned} \tag{20}$$

$$\mathbf{P}_{\text{g}} = \mathbf{F}\mathbf{S}_{\text{g}} = \mu J^{-\frac{2}{3}}\mathbf{F} - \big(\frac{\mu J^{-\frac{2}{3}} I_1}{3}\big)\mathbf{F}^{-T}. \tag{21}$$

To declutter the equations that follow, the scalars $G_i = \kappa J^{-\frac{2}{3}} I_1 + (1 - 3\kappa) J^{-\frac{2}{3}} I_i - 1$ with $i = 4, 6$, are introduced. Employing G_i and (18), the free energy associated with the fibres becomes

$$\begin{aligned} \psi_{\text{fib}}(\bar{\mathbf{C}}) &= \psi_{\text{fib},4}(\mathbf{C}) + \psi_{\text{fib},6}(\mathbf{C}), \\ \psi_{\text{fib}}(\mathbf{C}) &= \sum_{i=4,6} \frac{k_1}{2k_2} \left(\exp\left(k_2 G_i^2\right) - 1\right). \end{aligned} \tag{22}$$

The partial derivative of G_i with respect to $\mathbf{C}$ is

$$\begin{aligned} \frac{\partial G_i}{\partial \mathbf{C}} =& \kappa\left(\frac{\partial J^{-\frac{2}{3}}}{\partial \mathbf{C}} I_1 + J^{-\frac{2}{3}} \frac{\partial I_1}{\partial \mathbf{C}} \right) \\ &+ (1 - 3\kappa)\left(\frac{\partial J^{-\frac{2}{3}}}{\partial \mathbf{C}} I_i + J^{-\frac{2}{3}} \frac{\partial I_i}{\partial \mathbf{C}} \right) \\ =& \big(\kappa I_1 + (1 - 3\kappa) I_i\big)\big(-\frac{1}{3} J^{-\frac{2}{3}} \mathbf{C}^{-1} \big) \\ &+ \big(\kappa J^{-\frac{2}{3}}\big)\mathbf{I} + \big(1 - 3\kappa\big) J^{-\frac{2}{3}} A_i. \end{aligned} \tag{23}$$

Using (23), the stress response associated with the fibres is given by

$$\begin{aligned} \mathbf{S}_{\text{fib}} &= 2\frac{\partial \psi_{\text{fib}}}{\partial \mathbf{C}} = \sum_{i=4,6} \frac{k_1}{k_2} \left[(2k_2 G_i) \exp(k_2 G_i^2) \frac{\partial G_i}{\partial \mathbf{C}} \right], \\ \mathbf{P}_{\text{fib}} &= \mathbf{F}\mathbf{S}_{\text{fib}}. \end{aligned} \tag{24}$$

Weak form of the solid equations Taking the incompressibility into account and adapting the stationarity conditions in (16) for a dynamic setting, the weak form of the solid equations in the reference domain are given by

$$\begin{aligned} &\int_{\Omega_{\text{s}}} \big(\delta\mathbf{v} \cdot \rho_{\text{s}} \frac{\partial \mathbf{v}}{\partial t}\big)\mathrm{dV} + \int_{\Omega_{\text{s}}} \big(\nabla\delta\mathbf{v} : \mathrm{J}\mathbf{p}\mathbf{F}^{-1}\big)\mathrm{dV} \\ &\quad + \int_{\Omega_{\text{s}}} \big(\nabla\delta\mathbf{v} : \mathbf{P}\big)\mathrm{dV} - \int_{\Gamma_{\text{s}}} \big(\delta\mathbf{v} \cdot \mathbf{g}_{\text{s}}\big)\mathrm{dS} = 0 \quad \forall \delta\mathbf{v} \in H_D^1, \\ &\int_{\Omega_{\text{s}}} \big(\delta\mathbf{u} \cdot \frac{\partial \mathbf{u}}{\partial t}\big)\mathrm{dV} - \int_{\Omega_{\text{s}}} \big(\delta\mathbf{u} \cdot \mathbf{v}\big)\mathrm{dV} = 0 \quad \forall \delta\mathbf{u} \in H_D^1, \\ &\int_{\Omega_{\text{s}}} \delta p\big(J - 1\big)\mathrm{dV} = 0 \quad \forall \delta p \in L_D^2. \end{aligned} \tag{25}$$

2.2.3 Weak form of the mesh motion

The mesh motion is an artificial variable. On the interface, the Dirichlet boundary conditions for the mesh motion are given by (9_b-9_c). It would be unphysical if the mesh offered resistance to the vessel. To prevent this, a Dirichlet condition is implemented on the interface Γ_i ($\mathbf{u}_f = \mathbf{u}_s$) by requiring that $\delta\mathbf{u}$ vanish on the interface. The weak form of the mesh motion is thus given by

$$\int_{\Omega_f} \big(\nabla\delta\mathbf{u} : \alpha\,\mathrm{Grad}\,\mathbf{u}\big)\mathrm{dV} = 0 \quad \forall\delta\mathbf{u} \in \mathscr{V}^0_{\Gamma_i},$$

where $\mathscr{V}^0_{\Gamma_i} = H^1_{\mathrm{D,i}}(\mathbf{X}) = \big\{\mathbf{u} \in H^1(\mathbf{X}) : \mathbf{u} = \mathbf{0} \ \text{ on } \ \Gamma_i\big\}$.

2.2.4 Weak form of the coupling conditions

The coupling conditions are enforced in the following manner. Continuity of $\mathbf{v}$ across Γ_i is strongly enforced by using a continuous velocity field across the whole domain Ω. The continuity of normal stresses becomes an implicit condition by omitting the boundary integral jump, that is

$$\int_{\Gamma_i} (\delta\mathbf{v} \cdot J\sigma_s\mathbf{F}^{-T}\mathbf{n}_s)\mathrm{dS} = -\int_{\Gamma_i} (\delta\mathbf{v} \cdot J\sigma_f\mathbf{F}^{-T}\mathbf{n}_f)\mathrm{dS}.$$

2.3 Weak form in the reference domain

The residual of the equations developed in the previous section is written in the reference domain as follows:

$$\begin{aligned}
R(\mathbf{U};\delta\mathbf{v},\delta\mathbf{u},\delta p) = &\int_{\Omega_f} \delta\mathbf{v} \cdot J\rho_f \frac{\partial\mathbf{v}}{\partial t}\,\mathrm{dV} \\
&+ \int_{\Omega_f} \delta\mathbf{v} \cdot J\rho_f \big(\mathrm{Grad}\,\mathbf{v}\big)\mathbf{F}^{-1}(\mathbf{v} - \frac{\partial\mathbf{u}}{\partial t})\,\mathrm{dV} \\
&+ \int_{\Omega_f} \nabla\delta\mathbf{v} : J\sigma_f\mathbf{F}^{-T}\mathrm{dV} - \int_{\Gamma_f} \delta\mathbf{v} \cdot \mathbf{g}_f\,\mathrm{dS} \\
&+ \int_{\Omega_f} \delta p \cdot \mathrm{Div}\,\big(J\mathbf{F}^{-1}\mathbf{v}\big)\mathrm{dV} + \int_{\Omega_s} \delta\mathbf{v} \cdot \rho_s \frac{\partial\mathbf{v}}{\partial t}\mathrm{dV} \\
&+ \int_{\Omega_s} \big(\nabla\delta\mathbf{v} : Jp\mathbf{F}^{-1}\big)\mathrm{dV} + \int_{\Omega_s} \nabla\delta\mathbf{v} : \mathbf{P}\,\mathrm{dV} \\
&+ \int_{\Omega_s} \delta\mathbf{u}\frac{\partial\mathbf{u}}{\partial t}\mathrm{dV} - \int_{\Omega_s} \delta\mathbf{u} \cdot \mathbf{v}\,\mathrm{dV} \\
&+ \int_{\Omega_s} \delta p\big(J-1\big)\mathrm{dV} - \int_{\Gamma_s} \delta\mathbf{v} \cdot \mathbf{g_s}\,\mathrm{dS} \\
&+ \int_{\Omega_f} \nabla\delta\mathbf{u} : \big(\alpha\,\mathrm{Grad}\mathbf{u}\big)\mathrm{dV} \\
= 0 \qquad &\forall(\delta\mathbf{v},\delta\mathbf{u},\delta p) \in \mathscr{X}^0, \qquad (26)
\end{aligned}$$

where $\mathbf{U} = \{\mathbf{v},\mathbf{u},p\}$ and $\mathscr{X}^0 = H^1_{D,\mathrm{f},\mathbf{v}} \times H^1_{D,\Gamma_i,\mathrm{f},\mathbf{u}} \times L^2_{D,\mathrm{f},p}$.

2.4 Considerations at the outlet boundary

Outlet boundary conditions for cardiovascular applications are not trivial. As the boundary is computational (artificial) and not physical, the effect of the downstream vasculature on the domain needs to be taken into account. Waves should be able to travel through the domain without unphysical reflections. Backflow that occurs at the boundary should be captured but possible simulation divergence should be avoided.

2.4.1 Backflow Stabilization

Backflow is a physiological phenomenon commonly observed in complex geometries such as stenoses or anastomoses. Backflow stabilization provides convective flow information that is not present at an artificial outlet boundary, to preserve the flow features at the boundary without giving rise to numerical instabilities (Bazilevs et al, 2009; Braack et al, 2014; Moghadam et al, 2011). To include backflow stabilization, the traction boundary term $\int_{\Gamma_f} \big(\delta\mathbf{v} \cdot \mathbf{g}_f\big)\mathrm{dS}$ in the weak form of the momentum equation (11) is augmented for the outflow boundaries $\int_{\Gamma_{\mathrm{out}}}$. The backflow stabilization method adds an extra term to the traction outlet conditions that is only active when backflow is present. At the outlets the normal component of the stress is modified as follows:

$$\mathbf{n} \cdot \tilde{\sigma}\mathbf{n} + R_R \int_{\Gamma_{\mathrm{out}}} \mathbf{v} \cdot \mathbf{n}\,\mathrm{dS_t} + \mathrm{p_0} = 0, \qquad (27)$$

where R_R is the resistance of the downstream vasculature and

$$\tilde{\sigma}\mathbf{n} = -p\mathbf{n} + \rho_f\nu_f(\nabla\mathbf{v}\mathbf{F}^{-1} + \mathbf{F}^{-T}\nabla\mathbf{v}^T)\mathbf{n} - \rho_f\beta\mathbf{v}(\mathbf{v}\cdot\mathbf{n})_-. \qquad (28)$$

As discussed in the next section, the second term in (27) represents a pressure that is a function of the flow over the boundary. Here $0 < \beta < 1$, and $(\mathbf{v}\cdot\mathbf{n})_-$ denotes the part associated with back flow of $\mathbf{v}\cdot\mathbf{n}$; that is;

$$(\mathbf{v}\cdot\mathbf{n})_- = \begin{cases} \mathbf{v}\cdot\mathbf{n}, & \text{if } \mathbf{v}\cdot\mathbf{n} < 0, \\ 0, & \text{otherwise.} \end{cases} \qquad (29)$$

When applying the boundary condition this additional term must be added to the weak form of the fluid equations written in the reference configuration (11). Using Nanson's law, $\mathbf{n}\mathrm{dS_t} = J\mathbf{F}^{-\mathrm{T}}\mathbf{N}\,\mathrm{dS}$, the traction boundary term in $(11)_a$ is augmented by

$$\begin{aligned}
&-\int_{\Gamma_{\mathrm{out}}} \delta\mathbf{v} \cdot \rho_f\beta\mathbf{v}(\mathbf{v} \cdot J\mathbf{F}^{-T}\mathbf{N})_-\,\mathrm{dS} \\
&+ \big(\int_{\Gamma_{\mathrm{out}}} \delta\mathbf{v} \cdot J\mathbf{F}^{-T}\mathbf{N}\,\mathrm{dS}\big)\big(\mathrm{R_R}\int_{\Gamma_{\mathrm{out}}} \mathbf{v} \cdot J\mathbf{F}^{-\mathrm{T}}\mathbf{N}\,\mathrm{dS} + \mathrm{p_0}\big). \qquad (30)
\end{aligned}$$

The resistive boundary condition can be generalized so that any functional relationship between the normal stress and

blood flow rate can be prescribed in which case (27) becomes:

$$\mathbf{n}\cdot\bar{\sigma}\mathbf{n}+f(Q_{\text{out}})=0, \tag{31}$$

where

$$Q_{\text{out}}(\mathbf{v},\mathbf{F})=\int_{\Gamma_{\text{out}}}\mathbf{v}\cdot J\mathbf{F}^{-T}\mathbf{N}\,\mathrm{dS}. \tag{32}$$

The linearization of this boundary condition is discussed in Appendix 2.

2.4.2 Windkessel Model

The choice of outflow boundary conditions has a significant effect on both the velocity and the pressure fields of a 3D blood flow simulation. A common practice is to prescribe, neither the flow rate nor the pressure, but rather the functional relationship that exists between the pressure and flow. A lumped parameter model is used to describe the relation and can be directly coupled to the momentum equation (11). The lumped parameter models are described by ordinary differential equations (ODEs) that represent the dynamic description of the physics, whilst neglecting the spatial variation of its parameters and variables. By using the multi–domain method (Vignon-Clementel et al, 2006), these ODEs can be incorporated in the weak form of the governing equations. Apart from the resistive effects of the downstream vessels, the compliance of the vessels should also be taken into account.

We follow the implementation in Vignon-Clementel et al (2010) where a three–element Windkessel is used which consists of a resistance in series with a parallel configuration of a capacitance and resistance. The weak form and discretization of the Windkessel model are discussed in Appendix 3.

3 Numerical Implementation

3.1 Discretisation and Finite Element Approximation

To compute the numerical solution for the continuous fields $\mathbf{u},\mathbf{v},p$, the equations developed in the previous section are discretized in both time and space. We use Rothe's method and discretize first in time, and solve the resulting stationary PDE with finite element techniques.

To prevent spatial instability that may result for convection–dominated flows, streamline upwinding by the Petrov-Galerkin method (SUPG) is implemented (Brooks and Hughes, 1982). To eliminate possible oscillations in the solution, an artificial viscosity is added in the direction of the streamlines, and the modified residual in (26) is given by

$$\tilde{R}(\mathbf{U};\delta\mathbf{v},\delta\mathbf{u},\delta p)=R(\mathbf{U};\delta\mathbf{v},\delta\mathbf{u},\delta p)+S_{\text{stab}}(\mathbf{U};\delta\mathbf{v}). \tag{33}$$

More information on the choice of $S_{\text{stab}}(\mathbf{U};\delta\mathbf{v})$ is given in (Braack et al, 2007). This consistent formulation has a major drawback that comes from the necessity to compute second derivatives contained in the divergence of $J\sigma_{\text{f}}\mathbf{F}^{-T}$. For this reason we follow Wick (2015) and use a nonconsistent version and apply the stabilization only to the convective term; thus

$$S^{e}_{\text{stab}}=\left[J\rho_f\left(\text{Grad}\,\mathbf{v}\right)\mathbf{F}^{-1}\mathbf{v}\cdot\delta_K(\mathbf{v}\cdot\nabla)\delta\mathbf{v}\right]. \tag{34}$$

Time integration is done by using the Generalized–α method (Chung and Hulbert, 1993) as implemented for FSI by Kang et al (2012). The Generalized–α method allows damping while maintaining second–order accuracy.

The global residual (26) is discretized to find the approximate solution for all $n=1,2....N$

$$R(\mathbf{U}^n_h;\delta\mathbf{v}_h,\delta\mathbf{u}_h,\delta p_h)=0. \tag{35}$$

The nodal contributions are assembled to the global level and solved monolithically. Q^c_2/P^{dc}_1 finite elements are used to approximate the continuous unknowns and test functions. These comprise a continuous triquadratic element with 27 nodes for the displacement and velocity fields, and a discontinuous linear element with 4 nodes for the pressure field. The Q^c_2/P^{dc}_1 element is a good choice to impose incompressibility in the fluid and to prevent locking in the incompressible solid.

3.2 Linearization and the block structure of the equations

The discretized equations contain geometrical as well as material non–linearities. In addition, the convection term in the the fluid is nonlinear and the ALE map introduces non–linearity.

We employ Newton's method to solve the equations for each time step. Given an initial guess $\mathbf{U}^{n,0}_h$, find the update $\delta\mathbf{U}^{n,j}_h$ for $j=0,1,2,...:$

$$\begin{aligned} A(\mathbf{U}^{n,j}_h;\delta_h)\delta\mathbf{U}^{n,j}_h &= -R(\mathbf{U}^{n,j}_h;\delta_h), \qquad \forall\delta_h\in\mathscr{X}^0_h.\\ \mathbf{U}^{n,j+1}_h &= \mathbf{U}^{n,j}_h+\Lambda\,\delta\mathbf{U}^{n,j}_h. \end{aligned} \tag{36}$$

Λ is a damping parameter used for line search iterations (Wick, 2013). The tangents, $R_{D_{\Delta\mathbf{U}}}(\mathbf{U}^{n,j}_h)(\delta_h)$ are calculated using directional derivatives.

The linear system of equations (36) has the form $\mathbf{Ay}=\mathbf{b}$ where $\mathbf{A}$ denotes the tangent matrix, $\mathbf{b}$ the negative residual

vector and $\mathbf{y}$ the change in the solution vector. The block–structure of the linearized equation is given by

$$\begin{bmatrix} D_{vv,f} & 0 & D_{vu,f} & 0 & D_{vp,f} & 0 \\ 0 & D_{vv,s} & 0 & D_{vu,s} & 0 & D_{vp,s} \\ 0 & 0 & D_{uu,f} & 0 & 0 & 0 \\ 0 & D_{uv,s} & 0 & D_{uu,s} & 0 & 0 \\ D_{pv,f} & 0 & D_{pp,f} & 0 & 0 & 0 \\ 0 & 0 & 0 & D_{pu,s} & 0 & 0 \end{bmatrix} \begin{bmatrix} \delta \mathbf{v}_f \\ \delta \mathbf{v}_s \\ \delta \mathbf{u}_f \\ \delta \mathbf{u}_s \\ \delta p_f \\ \delta p_s \end{bmatrix} = - \begin{bmatrix} R_{\mathbf{v},f} \\ R_{\mathbf{v},s} \\ R_{\mathbf{u},f} \\ R_{\mathbf{u},s} \\ R_{p,f} \\ R_{p,s} \end{bmatrix}. \tag{36}$$

The expressions for the components of the tangent matrix are given in Appendix 1.

3.3 Initializing model with accurate biomechanical data

The geometry acquired from the MRI is in a configuration that is neither load– nor stress–free. To start the forward simulation, either the stress–free configuration (see Gee et al (2010)) or the pre-stress present in the reference configuration needs to be found (see Hsu and Bazilevs (2011)). We followed the latter approach to find the pre–stress $\mathbf{S}_0$. The first Piola–Kirchhoff stress tensor is calculated from $\mathbf{P} = \mathbf{F}(\mathbf{S} + \mathbf{S}_0)$. To determine $\mathbf{S}_0$, note that when $\mathbf{F} = \mathbf{I}$ or $\mathbf{u} = \mathbf{0}$ the body is in equilibrium with the traction applied to the interface Γ_i due to the blood flow. Consider now the weak quasi–static form of the balance of linear momentum in the solid (4). The symmetric pre–stress tensor $\mathbf{S}_0$ needs to be found such that for all $\delta\mathbf{u}$,

$$\int_{\Omega_s} \nabla\delta\mathbf{u} \cdot \mathbf{F}\mathbf{S}_0 \mathrm{dV} + \int_{\Gamma_{i,s}} \left(\delta\mathbf{u} \cdot \tilde{\mathbf{g}}\right) \mathrm{dS} = 0, \tag{37}$$

where $\tilde{\mathbf{g}}$ is the traction due to the fluid.

First $\tilde{\mathbf{g}}$ is approximated by using a rigid wall simulation with a physiologically realistic pressure applied at the outlet. This traction vector is applied incrementally on $\Gamma_{i,s}$. For each increment, $\mathbf{S}_0$ is found such that $\mathbf{u} = \mathbf{0}$ and thus $\mathbf{F} = \mathbf{I}$. This is done in an iterative manner, where for iteration n:

1. Update the pre–stress: $\mathbf{S}_0^n = \mathbf{S}_0^{n-1} + \mathbf{S}^{n-1}$
2. Solve for $\mathbf{u}$:

$$\int_{\Omega_s} \nabla\delta\mathbf{u} \cdot \mathbf{F}(\mathbf{S} + \mathbf{S}_0^n) \mathrm{dV} + \int_{\Gamma_{i,s}} \left(\delta\mathbf{u} \cdot \tilde{\mathbf{g}}\right) \mathrm{dS} = 0, \tag{38}$$

This is done until $\mathbf{u} \approx \mathbf{0}$, in which case $\mathbf{S}_0$ is the pre-stress in the converged stated and $\mathbf{S} \approx \mathbf{0}$. When the total pressure has been applied the forward simulation can commence.

The fibre directions are prescribed in the material model (17) by the angle between the local coordinate system and the fibre directions (Fig. 3). For a block or cylinder this is straightforward and the global Cartesian or cylindrical coordinate system can be used to define the local coordinate system and hence the fibre orientation. For a patient–specific geometry with vessel bifurcations a different strategy must be adopted.

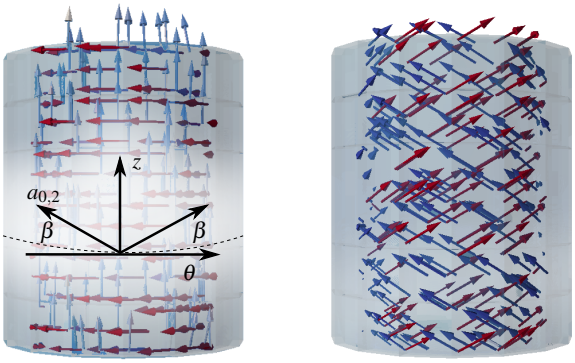

Fig. 3 The directions of the principal stresses (left) shown in red and blue and associated fibre directions (right) for a cylinder. β denotes the angle between the circumferential direction θ and the prescribed fibre direction.

The principal stress distribution of a cylindrical tube under internal pressure was studied by Alastrué et al (2010). They observed that the maximum principal stress is always positive and in the circumferential direction, the direction of the intermediate principal stress coincides with the axial line of the vessel and the minimum principal stress is aligned with the radial direction. These observations were used here to determine the local coordinate system for the arterial wall. The fibre orientation was included explicitly when calculating the pre–stress. After $\mathbf{S}_0$ was determined for each increment of the load, the principal stresses (eigenvalues) and directions of the principal stresses were obtained. With the directions of the principal stresses known, the fibre directions $\mathbf{a}_{0,i}$ can be determined for a known angle β (Fig. 3) .

3.4 Software

The algorithm described in the previous sections was implemented using the Differential Equation Analysis Library (deal.II) (Bangerth et al, 2007), an open-source C++ finite element toolkit and library. An existing 2D FSI code (Wick, 2013) was extended to 3D, parallelised and further extended to include the material model, boundary conditions and pre-stress algorithm. The full source code to implement the FSI model is available from de Villiers et al (2017).

4 Results

An overview of the experimental data used to validate the model, the setup, calibration and initialization of the model and an analysis of the results from the simulations, is now given.

4.1 Experimental data

Verification and validation of the mathematical model and numerical implementation of the FSI simulation are critical. To verify that the model was implemented correctly, several benchmark examples were created to test different parts of the code.

For model validation, data from 4D velocity encoded MRI was compared with the predicted flow in the fistula (Markl et al, 2011).

4D velocity acquisition employs phase contrast magnetic resonance to measure the velocity of the blood flow in the three spatial dimensions and the temporal dimension. It is a combination of 3D spatial encoding, three–directional velocity encoding and cine acquisition. The data it provides makes the visualization of the temporal evolution of complex flow patterns throughout a volume possible. The collection of these data sets relies on efficient synchronization relative to cardiac movements, which is achieved by electrocardiogram (ECG) gating. The time dimension of this cine velocity acquisitions does not represent real time but rather an effectively averaged heart cycle. This means that it does not capture any instabilities or beat–to–beat variations of the blood flow.

4.2 Setup and calibration of the model

The geometry of the patient–specific fistula is acquired from the MRI data and converted to a computational mesh in the following steps. First, the extracted geometry is transformed into a point cloud representation using the 4D Flow tool (Siemens AG). The point cloud data is then converted into an STL format using Meshlab (Cignoni et al., 2008). The STL file is then imported into the meshing software ANSA (BETA, 2009) and the hexablock tool used to create a mesh of hexahedral elements suitable for the analysis in deal.II.

The mesh contains information that identifies the different materials for each hexahedral element. Different boundaries can also be identified. Fig. 4 shows the various material regions.

Fig. 5 shows the change in cross–sectional area of a vessel due to an applied interior pressure. The experimental data are for the smooth muscle of the brachial arterial wall relaxed with nitroglycerin (Bank et al, 1999) and from in vitro experiments performed on porcine carotid arteries (Kaiser et al, 2001; Roy et al, 2005). There is a lack of experimental data and although these experiments do not supply enough information for an accurate description of the human brachial artery, it gives a realistic indication of the response of the artery to an applied pressure. The data were used to calibrate the constitutive model for the arterial wall, with the simulated results shown in Fig. 5.

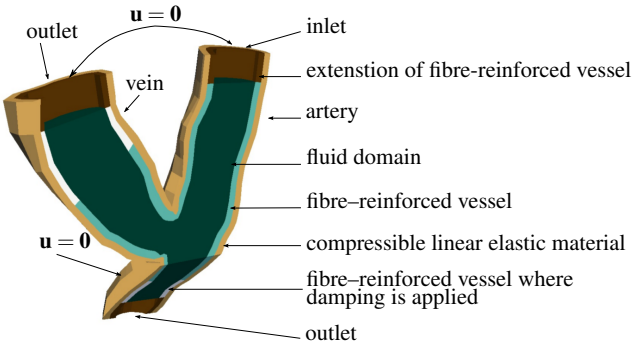

Fig. 4 The various computational domains and boundaries of the fistula.

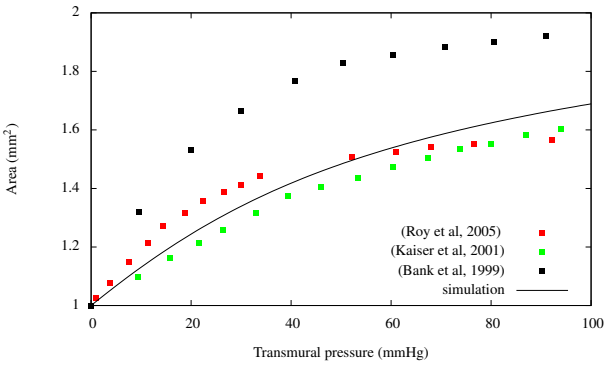

Fig. 5 The experimental relation between the cross–sectional area and the transmural pressure, and the results of the simulation with the calibrated material parameters.

The blood is described by its density $\rho_f = 1060\ \mathrm{kg/m^3}$ and viscosity $\nu_f = 4.0 \times 10^{-6}\ \mathrm{m^2/s}$. The fibre–reinforced vessel has a density $\rho_s = 1000\ \mathrm{kg/m^3}$, Lamé's first parameter $\lambda = 38200$ Pa, the first and second fibre constants $k_1 = 199320$ Pa and $k_2 = 108.4$, the local fibre direction $\beta = 49.98^o$ and the dispersion parameter $\kappa = 0.226$. These values are all physically realistic (Gasser et al, 2006; Kenner, 1989; Shirazian et al, 2012).

The fibre–reinforced vessel is extended beyond the fluid domain at the inlet and outlets as depicted in Fig. 4. The ends of these extensions are fixed in space. This allows displacement in both the radial and axial directions at the inlets and outlets of the fluid domain.

The vessel is surrounded by a compressible isotropic linear elastic material that represents the soft tissue. This provides resistance against bending of the vessel. The soft tissue material is defined by Lamé's first parameter $\lambda = 38200$ Pa and Poisson's ratio $\nu_s = 0$. The boundary on the outside of the linear elastic material is fixed.

Flow at the inlet is prescribed using the MRI data (Fig. 6). The MRI data also provide information on the flow downstream of the bifurcation. The flow division was computed from the 4D MRI data. The Windkessel values are fitted to

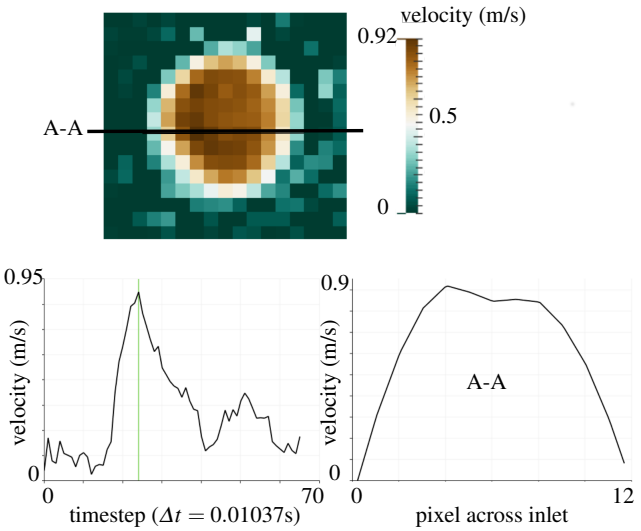

Fig. 6 Prescribing the flow at the inlet. (a) a processed image from MRI; (b) the velocity at a point on the inlet over the period of a heartbeat; (c) the velocity profile across the artery at $t = 0.249$ s.

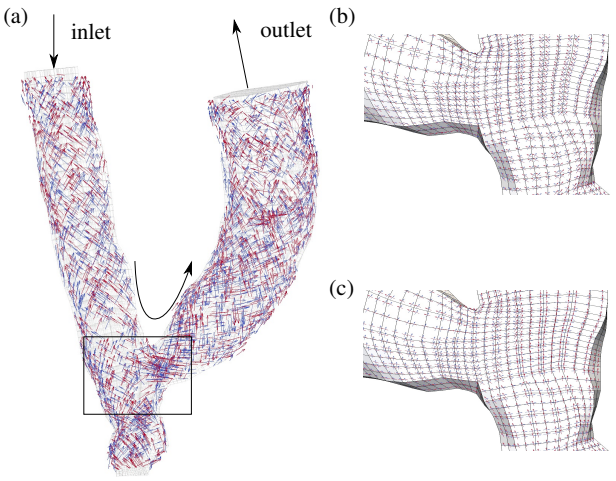

Fig. 7 (a) The fibre directions for a patient–specific geometry. (b) Fibre directions at the anastomosis. (c) Directions of the maximum principal stress and mid principal stress, used to find the circumferential and axial directions, respectively.

this division of flow, and to pressure data found in the literature.

There is little data available on the pressure in brachial–cephalic fistulas. Cuff pressure cannot be measured on the arm where the fistula is situated as the increased pressure may rupture the vein. Corpataux et al (2002) measured pressure for a patient at the end of the fistula creation operation before removing the intra–vascular catheter. The systolic and diastolic pressures measured were 50 and 20 mmHg respectively. These were for a fistula created in the radial artery, which is distal to the brachial artery. Safar et al (2002) measured the cuff pressure on the other arm for 110 patients. The mean systolic and diastolic were 151 and 86 mmHg respectively. Ash et al (2012) determined the intra–access pressure ratio in fistulas and grafts. The ratio between the cuff pressure and the pressure present in the fistula was found to be in the range 0.15-0.2. These values were determined from patients with different fistulas (radial–cephalic or brachial–basilic) and grafts. Using the intra–access pressure ratio values and the cuff pressure measure in Safar et al (2002), a physically realistic range for both the systolic (22.65-30.2 mmHg) and diastolic pressure (12.9-17.2 mmHg) in the brachial vein was obtained.

Table 1 shows the values of the parameters used in the Windkessel model. These values were chosen to achieve the desired flow division and will be discussed in Section 4.4.

	R Pa s/m^3	R_d Pa s/m^3	C m^3/(Pa s)	τ
Artery	1.35×10^7	2.02×10^8	4.94×10^{-9}	0.99
Vein	2.68×10^9	1.46×10^{10}	6.24×10^{-11}	0.91

Table 1 Windkessel parameters

4.3 Initializing the computational model

4.3.1 Fibre directions

The computed fibre directions in the reference domain $\mathbf{a}_{0,i}$ of a patient–specific fistula are shown in Fig. 7 (a). At the anastomosis a smooth transition of the direction of the fibres (Fig. 7 (b)) and of the principal stresses (Fig. 7 (c)) is clear.

4.3.2 Pre–stress

Fig. 8 shows the increase in pre–stress with the increment in pressure that is applied at the outlets of the fluid domain. At the top of the figure, the element average of the Frobenius norm of the stress is shown. This is the total stress, i.e. the sum of the pre–stress and stress related to the strain $\mathbf{S}_{\text{tot}} = \mathbf{S}_0 + \mathbf{S}$. The series of images at the bottom of Fig. 8 demonstrate how the displacement, and therefore strain, decreases when the stress is added to the pre–stress at each iteration $\mathbf{S}_0^n = \mathbf{S}_0^{n-1} + \mathbf{S}^n$ for a constant applied pressure. For each increment in the load the pre–stress algorithm is solved until the displacement becomes negligible ($\| \mathbf{u} \| \approx 0$).

4.4 Outflow

Figure 9 compares the outflow data from the MRI at the venous and arterial outlets to the simulation. The flow from the simulation at both of the outlets is of the same order as that from the MRI. The outflow profile at the outlets follows the same pattern over time and are of the same order of magnitude. The error in the flow, $\varepsilon = \frac{\sqrt{\int (Q_{\text{mri}} - Q_{\text{fe}})^2 \text{dt}}}{\int \text{dt}}$ at the prox-

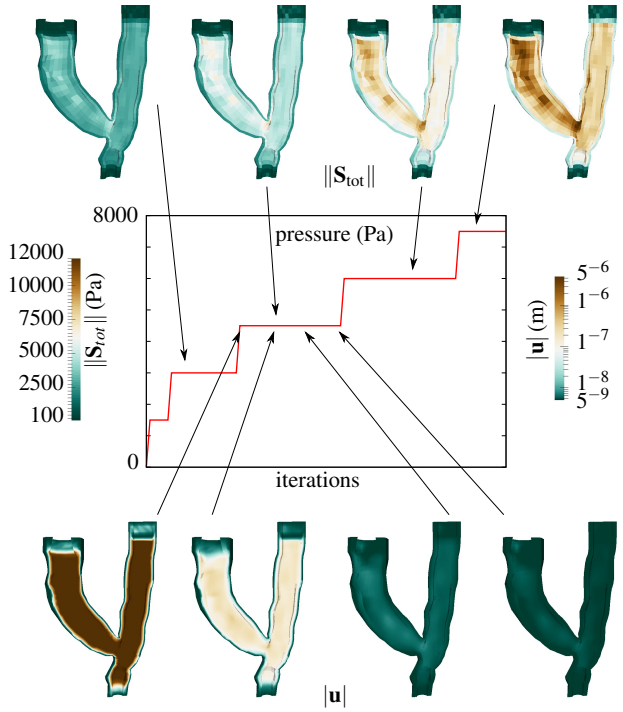

Fig. 8 Demonstration of the pre–stress algorithm. The pre–stress increase as the pressure applied at the outlet of the fluid boundary increase. During each iteration the displacements in the vessel and elastic material decrease.

imal and distal outlets are calculated as $\varepsilon_{\text{prox}} = 1.22 \times 10^{-5}$ m^3/s and $\varepsilon_{\text{dist}} = 2.16 \times 10^{-6}$ m^3/s.

4.5 Validation

To evaluate the reliability of the prediction of the finite element code, the flow fields from the simulations are compared to the flow data obtained from MRI.

When assessing whether the computational model is reasonable, the sources of inaccuracy from the processed MRI data should be kept in mind. These inaccuracies are a result of the resolution in both space and time. When comparing velocities obtained from the 4D MRI to velocities obtained from 3D MRI (2D in space and time; with higher resolution both in space and time) of slices at the inlet, outlet and anastomosis, the former velocities were considerably smaller. These differences were not uniform (i.e. there is a significant amount of spatial variation).

Figures 10 and 11 display 3D streamlines superimposed on a translucent image of the geometry. Note that the domain from the MRI shown in Fig. 11 is truncated for the simulation. The scaling of the images are different, but the dimensions of the bifurcation are the same. Also note that the visualizations for the MRI data and simulation were created by different software. Two different dynamic ranges were chosen to allow comparisons of both the lower and the higher velocity flow patterns. The low dynamic range (Fig. 10) highlights the recirculation at the heel of the anastomosis. The high dynamic range (Fig. 11) highlights the flow patterns with higher velocity at the foot of the anastomosis. Although the 4D MRI data contains inaccuracies and can not be used for a quantitative comparison, it is valuable to compare general flow features. The predictions of the recirculation in the vein, the very high flow in the anastomosis, and spiral flow in the artery distal to the anastomosis compare well with those obtained from the MRI.

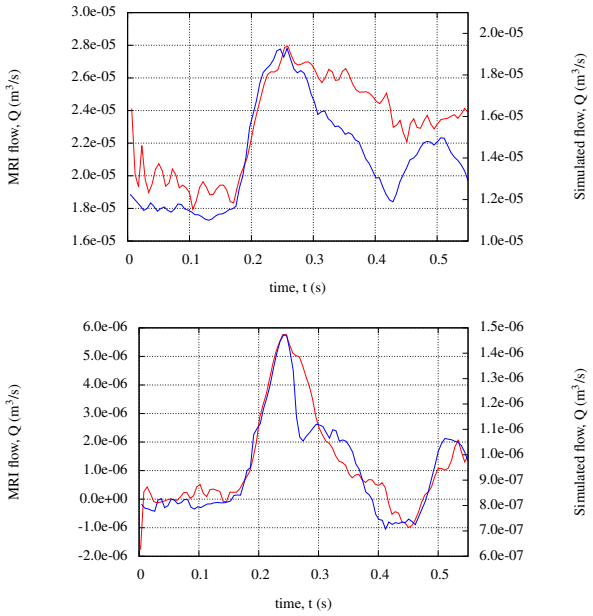

Fig. 9 Flow at the venous (top) and arterial (bottom) outlets obtained from MRI (red) and simulation (blue).

4.6 Analysis

There is certain information that can not be obtained from the MRI data, but which the simulation is able to provide. The WSS, oscillatory shear index (OSI), stress in the wall and propagation of the pressure wave are such information. The WSS is given by

$$\text{WSS} = \sigma_{\text{f}}\mathbf{n}_{\text{f}} - ((\sigma_f \mathbf{n}_{\text{f}}) \cdot \mathbf{n}_{\text{f}})\mathbf{n}_{\text{f}}, \tag{39}$$

and the OSI by

$$\text{OSI} = 0.5\left(1 - \frac{\left|\int_0^{\text{T}} \text{WSS}\,\text{dt}\right|}{\int_0^{\text{T}} |\text{WSS}|\,\text{dt}}\right). \tag{40}$$

Here T is the time at the end of a heart cycle. The WSS is relatively low in most of the fistula, but a section of very

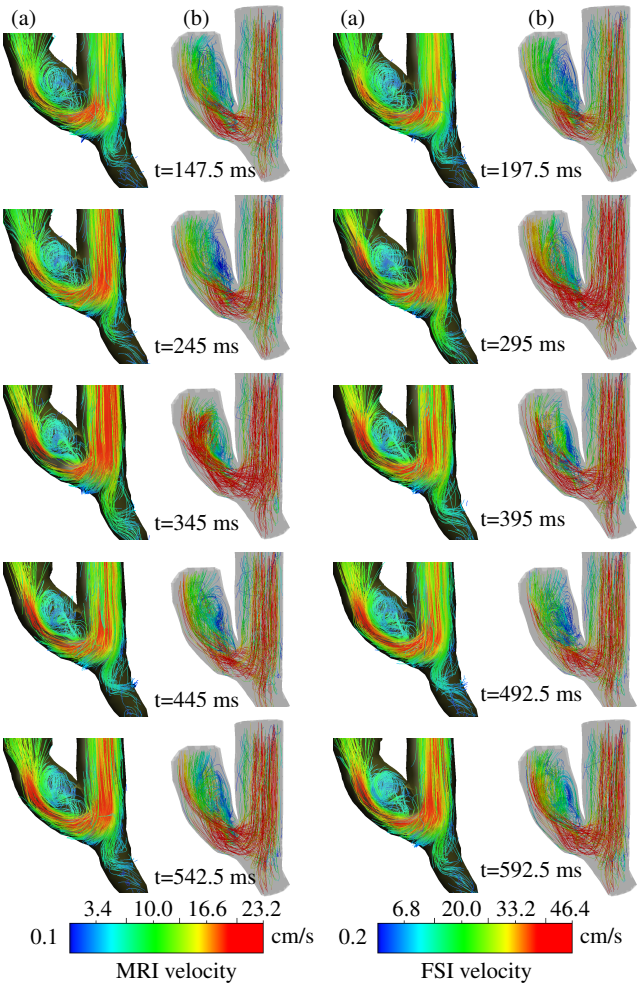

Fig. 10 Comparing volume streamlines in the low dynamic range from (a) MRI to (b) simulation at different times. The 3D streamlines are displayed over a transclucent geometry.

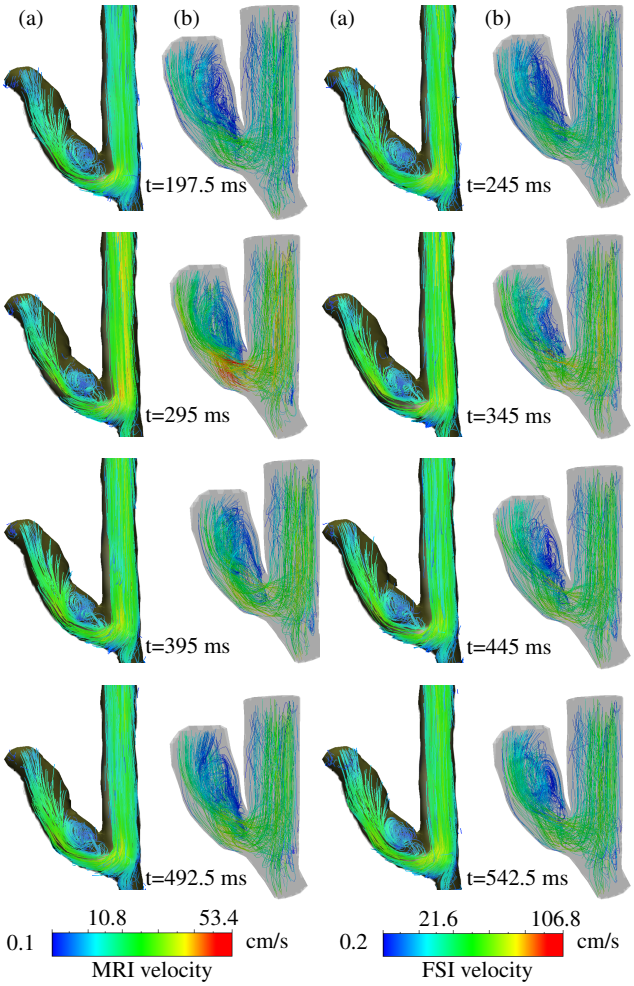

Fig. 11 Comparing volume streamlines in the high dynamic range from (a) MRI to (b) simulation at different times. The 3D streamlines are displayed over a transclucent geometry.

high shear stress is present at the anastomosis (Fig. 12 (a) and Fig. 15). The maximum shear stress computed over the entire cycle and geometry, is more than 30 times higher than the maximum normal physiological WSS in veins and 10 times higher than the normal physiological WSS in large arteries (Kroll et al, 1996). WSS values of higher than 35 Pa (Fry, 1968) and lower than 0.2 Pa (Meyerson et al, 2001) are associated with the intimal hyperplasia. At the toe of the anastomis the WSS is greater than 35 Pa.

Regions of high OSI (> 0.4) can be seen at the heel of the fistula, the fistula bed (or side–wall) and in the region where WSS is lower than the physiological range as a result of the recirculation (Fig. 12 (b)). It has been shown that regions in which high oscillations in WSS are present are associated with the formation of atheroma (Cunningham and Gotlieb, 2005). It has also been shown that when other systemic risk factors are present, altered flow patterns promote atherosclerosis (Cunningham and Gotlieb, 2005).

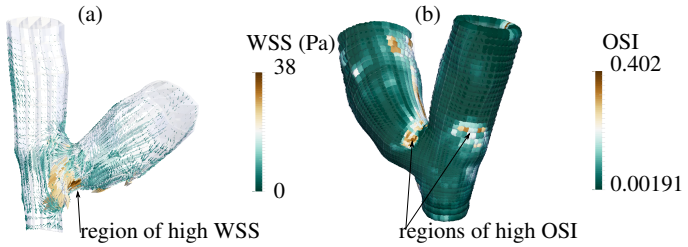

Fig. 12 (a) WSS and (b) OSI present in fistula at peak systole (t=295 ms).

The regions in which the WSS values are above and below the acceptable range or where the OSI values are high, indicate regions where intimal hyperplasia (IH) and atheroma may occur. IH and atheroma may lead to thrombosis (clots that form) which in turns leads to stenosis or embolism.

One of the strengths of using FSI is the ability to track the propagation and reflection of pressure waves, as shown

in Fig. 13 using pressure contours. The figure highlights the propagation of two waves. The blue indicator follows a pressure wave propagating through the venous side of the anastomosis and the red indicator follows a wave propagating through the artery; the wave is partially reflected at the anastomosis. There is a region of low pressure visible at the heel of the anastomosis and a high pressure region at the toe of the anastomosis. These are the regions mostly associated with the formation of intimal hyperplasia.

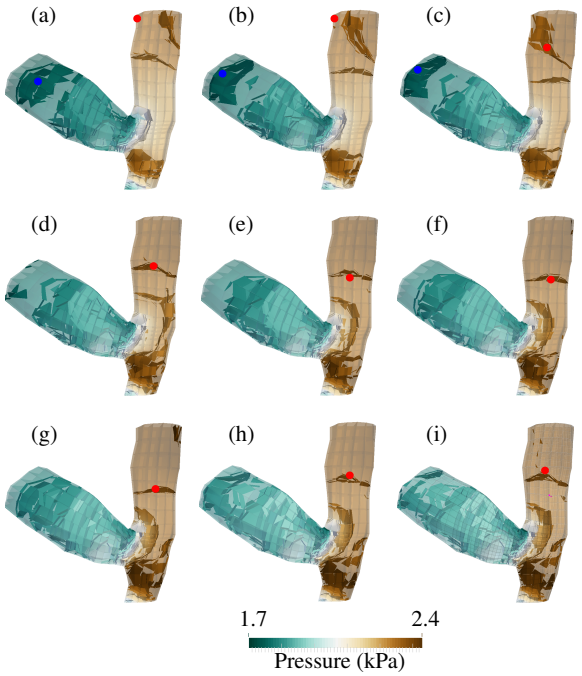

Fig. 13 Wave propagation for a period of 0.0038 s. The pictures show consecutive timesteps from left to right starting at the top row. The blue circle labels a wave propagating through the vein. The red circle labels a wave propagating through the artery, and reflected at the anastomosis.

4.7 Further applications of the computational model

The computational model can be used to analyse other patient–specific fistulas. A geometry has been created from MRI data of a different patient. In the absence of velocity data for the patient concerned, velocity data from the patient discussed in the previous section are used as inlet conditions. Results from the simulations at peak systole are presented. The streamlines in Fig. 14 shows recirculation in the vein and in the artery distal to the anastomosis. The velocities in the vein are low.

High WSS values are found in the artery and at the toe of the anastomosis. Low WSS values are found in the vein, especially at the bottom of the bulge in the vein where the

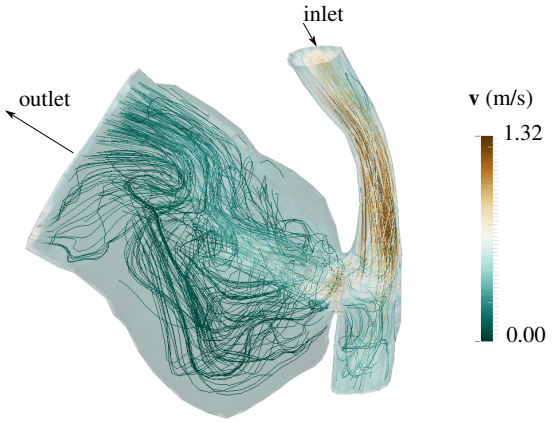

Fig. 14 Streamlines in fistula at peak systole.

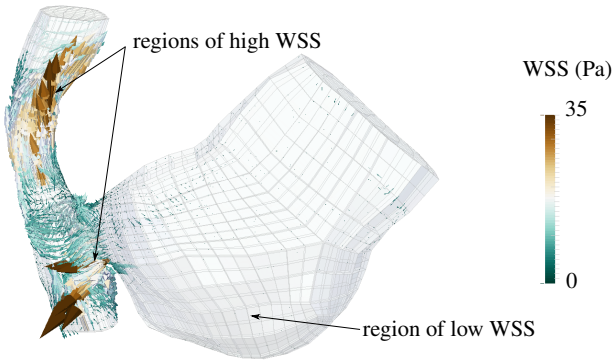

Fig. 15 Spatial distribution of WSS in fistula at peak systole.

WSS is lower than 0.2 Pa (Fig. 15). Thus there are regions of both high and low WSS that fall in the range associated with IH. The regions where the WSS is very high or very low correspond to the regions of high or low WSS values in the patient discussed in the previous section.

In regions where flow recirculation in the vein is seen, high OSI values are found (Fig. 16). At the heel of the anastomosis OSI values are also high. The areas of high OSI are similar to the regions of high OSI in the patient discussed in the previous section.

5 Discussion

A 3D parallelized FSI finite element model to simulate blood flow in fistulas was presented. Attention has been given to creating and using a patient–specific geometry for the simulations. The code was validated against flow data processed from velocity encoded MRI.

Various open source FE applications of the deal.ii library (Pelteret and McBride, 2016; Wick, 2013) have been extended to account for:

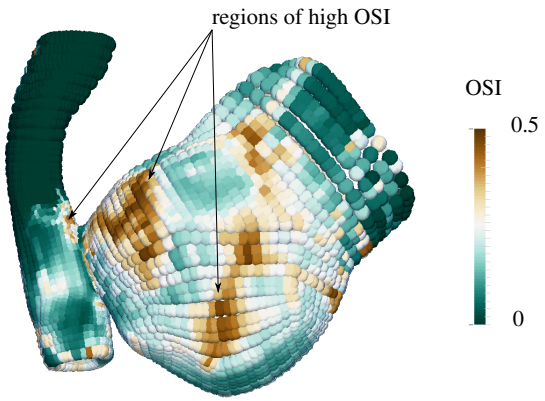

Fig. 16 Spatial distribution of OSI in fistula at peak systole.

- the 3D geometry,
- parallelized computation,
- classes and functions necessary to store relevant data at certain boundaries, to integrate the flow over the boundary and to calculate and store the Windkessel–values,
- classes and functions required to calculate WSS and OSI at the interface,
- classes and functions that calculate the fibre–directions and pre–stress.

Although many FSI codes and studies on haemodynamics and vascular mechanics exist, most have not been validated by in vivo data. This study has incorporated experimental data obtained from velocity encoded 4D MRI. The flow data from the MRI contain inaccuracies and the limited spatial resolution prevents an accurate determination of the boundary of the vessel. The cross–sectional area and consequently the flow calculated from the MRI thus contain some errors. The velocity dynamic range of the MRI data depends on the velocity encoding (VENC) setting. The VENC reflects the maximum velocity expected. If the VENC setting is 150 cm/s, velocities up to $\pm$ 150 cm/s can be captured without phase aliasing. The higher the VENC setting, the more difficult it is to capture small velocity differences. If however the VENC settings are not high enough to capture the velocity, phase wrapping occurs and incorrect values are assigned to the velocity values that fall outside the acceptable range. Flow at the boundaries is slow and therefore difficult to capture, adding to greater inaccuracy in the flow calculations. Furthermore, at the resolution of the MRI data there may be significant partial volume effects whereby a mix of velocities is represented in image voxels. For small arteries and veins such as the brachial artery and cephalic vein, these inaccuracies, although not numerically quantified, can be significant (Gatehouse et al, 2005). Although it is difficult to perform a quantitative comparison, the flow patterns from the simulation show very good qualitative agreement with those obtained from the MRI.

Regions of very high and low WSS and high OSI correspond to regions where IH occur. A region of high WSS ($>$ 35 Pa) is present in both patients at the toe of the anastomosis. A region of high OSI (> 0.4) is present at the heel of the anastomosis. High OSI values are also found where there is flow recirculation, especially in the vein. These correlations correspond to those found in CFD studies with regard to high (Carroll et al, 2009) and low WSS (Browne et al, 2014; Ene-Iordache and Remuzzi, 2012; McGah et al, 2014) and high values of OSI (Decorato et al, 2011; Ene-Iordache and Remuzzi, 2012).

Fistulas created in the upper arm that connect the cephalic vein to the brachial artery may be the last resort for patients with end stage renal disease. It is important to create the fistula in such a way that the patency rate is as high as possible. Understanding the flow and stress inside the fistula will contribute to the improvement of haemodialysis procedures. The FSI model is a starting point for further investigations into critical design features such as the angle of connection, the connection site of the fistula and the influence of WSS, OSI and stress in the vessel wall.

To make this FSI code clinically usable, the time necessary to run a simulation needs to be decreased. To achieve this an iterative solver and pre–conditioner should be implemented (see for example Heil (2004)). Adaptive time-stepping may decrease the simulation time by increasing the time-step size in the temporal regions far from the systolic pressure.

To calibrate the Windkessel parameters more accurately, better flow data are necessary.

The effect of shear thinning and other nonlinear features of blood at low shear rates, should be investigated (Zhuang et al, 1998).

In order to make general conclusions and recommendations for fistula creation. the study should be extended to include more patients.

To be able to assist in surgical planning, a temporal study needs to be done and remodelling of the vessels included (Manini et al, 2014). The 3D model should be included in a closed 1D model of the arterial network to predict the flow increase resulting from creating the fistula. Such a simulation tool might assist predicting whether the fistula will mature, and can make a prediction on the patency of the fistula to enable early intervention.

The freely-available, extensible computational model is a validated framework upon which to develop predictive computational simulations of AV access fistulas in order to improve their failure rate. The model can be extended to other AV access, and vascular connections in other interventions such as organ transplants and might ultimately lead to simulation based guides for clinical decision making.

Acknowledgements

The work by AMdV, ATMcB and BDR has been supported by the National Research Foundation of South Africa through the South African Research Chair in Computational Mechanics. This support is acknowledged with thanks.

The authors acknowledge and thank Delawir Kahn, Jennifer Downs, Ernesta Meintjies and Stephen Jermy for their contribution, which include project management, and capturing and processing the MRI scans.

Conflict of Interest: The authors declare that they have no conflict of interest.

References

Alastrué V, Garía A, Peña E, Rodríguez JF, Martínez MA, Doblaré M (2010) Numerical framework for patient-specific computational modelling of vascular tissue. International Journal for Numerical Methods in Biomedical Engineering 26(1):35–51

Allon M, Robbin ML (2002) Increasing arteriovenous fistulas in hemodialysis patients: problems and solutions. Kidney International 62(4):1109–1124

Ash SR, Dhamija R, Zaroura MY, Hentschel DM (2012) The StenTec gauge for measuring static intra-access pressure ratio (PIa ratio) of fistulas and grafts. In: Seminars in dialysis, Wiley Online Library, Blackwell Publishing Ltd., vol 25, pp 474–481

Bangerth W, Hartmann R, Kanschat G (2007) deal. II-a general-purpose object-oriented finite element library. ACM Transactions on Mathematical Software (TOMS) 33(4):24

Bank AJ, Kaiser DR, Rajala S, Cheng A (1999) In vivo human brachial artery elastic mechanics effects of smooth muscle relaxation. Circulation 100(1):41–47

Bazilevs Y, Gohean JR, Hughes TJR, Moser RD, Zhang Y (2009) Patient-specific isogeometric fluidstructure interaction analysis of thoracic aortic blood flow due to implantation of the Jarvik 2000 left ventricular assist device. Computer Methods in Applied Mechanics and Engineering 198(45):3534–3550

Boghosian M, Cassel K, Hammes M, Funaki B, Kim S, Qian X, Wang X, Dhar P, Hines J (2014) Hemodynamics in the cephalic arch of a brachiocephalic fistula. Medical engineering & physics 36(7):822–830

Bozzetto M, Ene-Iordache B, Remuzzi A (2016) Transitional flow in the venous side of patient-specific arteriovenous fistulae for hemodialysis. Annals of biomedical engineering 44(8):2388–2401

Braack M, Burman E, John V, Lube G (2007) Stabilized finite element methods for the generalized oseen problem. Computer Methods in Applied Mechanics and Engineering 196(4):853–866

Braack M, Mucha PB, Zajaczkowski WM (2014) Directional do-nothing condition for the navier-stokes equations. J Comput Math 32(5):507–521

Brooks AN, Hughes TJ (1982) Streamline upwind/petrov-galerkin formulations for convection dominated flows with particular emphasis on the incompressible navier-stokes equations. Computer Methods in Applied Mechanics and Engineering 32(1):199–259

Browne LD, OCallaghan S, Hoey DA, Griffin P, McGloughlin TM, Walsh MT (2014) Correlation of hemodynamic parameters to endothelial cell proliferation in an end to side anastomosis. Cardiovascular Engineering and Technology 5(1):110–118

Carroll GT, McGloughlin TM, OKeeffe LM, Callanan A, Walsh MT (2009) Realistic temporal variations of shear stress modulate mmp-2 and mcp-1 expression in arteriovenous vascular access. Cellular and Molecular Bioengineering 2(4):591

Causin P, Gerbeau JF, Nobile F (2005) Added-mass effect in the design of partitioned algorithms for fluid–structure problems. Computer methods in applied mechanics and engineering 194(42):4506–4527

Chung J, Hulbert GM (1993) A time integration algorithm for structural dynamics with improved numerical dissipation: the generalized-α method. Journal of Applied Mechanics 60(2):371–375

Corpataux JM, Haesler E, Silacci P, Ris HB, Hayoz D (2002) Low-pressure environment and remodelling of the forearm vein in Brescia–Cimino haemodialysis access. Nephrology Dialysis Transplantation 17(6):1057–1062

Cunnane CV, Cunnane EM, Walsh MT (2017) A review of the hemodynamic factors believed to contribute to vascular access dysfunction. Cardiovascular Engineering and Technology pp 1–15

Cunningham KS, Gotlieb AI (2005) The role of shear stress in the pathogenesis of atherosclerosis. Laboratory investigation 85(1):9–23

de Villiers A, McBride AT, Reddy BD (2017) Fsi fistula. DOI 10.5281/zenodo.437473, URL https://doi.org/10.5281/zenodo.437473

Decorato I, Kharboutly Z, Legallais C, Salsac AV (2011) Numerical study of the influence of wall compliance on the haemodynamics in a patient-specific arteriovenous fistula. Computer Methods in Biomechanics and Biomedical engineering 14(sup1):121–123

Ene-Iordache B, Remuzzi A (2012) Disturbed flow in radial-cephalic arteriovenous fistulae for haemodialysis: low and oscillating shear stress locates the sites of stenosis. Nephrology Dialysis Transplantation 27(1):358–368

Fry DL (1968) Acute vascular endothelial changes associated with increased blood velocity gradients. Circulation

research 22(2):165–197

Gasser TC, Ogden RW, Holzapfel GA (2006) Hyperelastic modelling of arterial layers with distributed collagen fibre orientations. Journal of the Royal Society Interface 3(6):15–35

Gatehouse PD, Keegan J, Crowe LA, Masood S, Mohiaddin RH, Kreitner KF, Firmin DN (2005) Applications of phase-contrast flow and velocity imaging in cardiovascular mri. European radiology 15(10):2172–2184

Gee M, Förster C, Wall W (2010) A computational strategy for prestressing patient-specific biomechanical problems under finite deformation. International Journal for Numerical Methods in Biomedical Engineering 26(1):52–72

Hammes M, Boghosian M, Cassel K, Watson S, Funaki B, Doshi T, Akherat SJM, Hines J, Coe F (2016) Increased inlet blood flow velocity predicts low wall shear stress in the cephalic arch of patients with brachiocephalic fistula access. PloS one 11(4):e0152,873

Haruguchi H, Teraoka S (2003) Intimal hyperplasia and hemodynamic factors in arterial bypass and arteriovenous grafts: a review. Journal of Artificial Organs 6(4):227–235

Heil M (2004) An efficient solver for the fully coupled solution of large-displacement fluid-structure interaction problems. Computer Methods in Applied Mechanics and Engineering 193(1):1–23

Holzapfel GA (2002) Nonlinear solid mechanics: a continuum approach for engineering science. Meccanica 37(4):489–490

Holzapfel GA, Gasser TC, Ogden RW (2000) A new constitutive framework for arterial wall mechanics and a comparative study of material models. Journal of Elasticity and the Physical Science of Solids 61(1-3):1–48

Hsu MC, Bazilevs Y (2011) Blood vessel tissue prestress modeling for vascular fluid-structure interaction simulation. Finite Elements in Analysis and Design 47(6):593–599

Huberts W, Canneyt KV, Segers P, Eloot S, Tordoir JHM, Verdonck P, van de Vosse FN, Bosboom EMH (2012) Experimental validation of a pulse wave propagation model for predicting hemodynamics after vascular access surgery. Journal of Biomechanics 45(9):1684–1691

Hughes TJR, Liu WK, Zimmermann TK (1981) Lagrangian-Eulerian finite element formulation for incompressible viscous flows. Computer Methods in Applied Mechanics and Engineering 29(3):329–349

Iori F, Grechy L, Corbett R, Gedroyc W, Duncan N, Caro C, Vincent P (2015) The effect of in-plane arterial curvature on blood flow and oxygen transport in arterio-venous fistulae. Physics of Fluids 27(3):031,903

Kaiser DR, Mullen K, Bank AJ (2001) Brachial artery elastic mechanics in patients with heart failure. Hypertension 38(6):1440–1445

Kang S, Choi H, Yoo JY (2012) Investigation of fluid–structure interactions using a velocity-linked P2/P1 finite element method and the generalized-α method. International Journal for Numerical Methods in Engineering 90(12):1529–1548

Kenner T (1989) The measurement of blood density and its meaning. Basic research in cardiology 84(2):111–124

Kharboutly Z, Deplano V, Bertrand E, Legallais C (2010) Numerical and experimental study of blood flow through a patient-specific arteriovenous fistula used for hemodialysis. Medical engineering & physics 32(2):111–118

Kroll MH, Hellums JD, McIntire L, Schafer A, Moake J (1996) Platelets and shear stress. Blood 88(5):1525–1541

Lee SW, Smith DS, Loth F, Fischer PF, Bassiouny HS (2007) Importance of flow division on transition to turbulence within an arteriovenous graft. Journal of Biomechanics 40(5):981–992

Malik J, Tuka V, Tesar V (2009) Local hemodynamics of the vascular access for hemodialysis. Kidney and Blood Pressure Research 32(1):59–66

Manini S, Passera K, Huberts W, Botti L, Antiga L, Remuzzi A (2014) Computational model for simulation of vascular adaptation following vascular access surgery in haemodialysis patients. Computer Methods in Biomechanics and Biomedical Engineering 17(12):1358–1367

Markl M, Kilner PJ, Ebbers T (2011) Comprehensive 4D velocity mapping of the heart and great vessels by cardiovascular magnetic resonance. J Cardiovasc Magn Reson 13(7):10–1186

McGah PM, Leotta DF, Beach KW, Aliseda A (2014) Effects of wall distensibility in hemodynamic simulations of an arteriovenous fistula. Biomechanics and modeling in mechanobiology 13(3):679–695

Meyerson SL, Skelly CL, Curi MA, Shakur UM, Vosicky JE, Glagov S, Christen T, Gabbiani G, Schwartz LB (2001) The effects of extremely low shear stress on cellular proliferation and neointimal thickening in the failing bypass graft. Journal of vascular surgery 34(1):90–97

Moghadam ME, Bazilevs Y, Hsia TY, Vignon-Clementel IE, Marsden AL, et al (2011) A comparison of outlet boundary treatments for prevention of backflow divergence with relevance to blood flow simulations. Computational Mechanics 48(3):277–291

Ngoepe MN, Reddy BD, Kahn D, Meyer C, Zilla P, Franz T (2011) A numerical tool for the coupled mechanical assessment of anastomoses of PTFE arterio-venous access grafts. Cardiovascular Engineering and Technology 2(3):160–172

Niemann AK, Udesen J, Thrysoe S, Nygaard JV, Frund ET, Petersen SE, Hasenkam JM (2010) Can sites prone to flow induced vascular complications in a-v fistulas be assessed using computational fluid dynamics? Journal of Biomechanics 43(10):2002–2009

Pelteret JP, McBride A (2016) The step–44 tutorial program. URL *http://www.dealii.org/8.4.1/doxygen/deal.II/step_44.html*

Roy S, Silacci P, Stergiopulos N (2005) Biomechanical proprieties of decellularized porcine common carotid arteries. American Journal of Physiology-Heart and Circulatory Physiology 289(4):H1567–H1576

Ryou HS, Kim S, Ro K (2013) A numerical study of the effect of catheter angle on the blood flow characteristics in a graft during hemodialysis. Korea-Australia Rheology Journal 25(1):19–27

Safar ME, Blacher J, Pannier B, Guerin AP, Marchais SJ, Guyonvarch PM, London GM (2002) Central pulse pressure and mortality in end-stage renal disease. Hypertension 39(3):735–738

Shirazian S, Rios-Rojas L, Drakakis J, Dikkala S, Dutka P, Duey M, Cho DJ, Fishbane S (2012) The effect of hemodialysis ultrafiltration on changes in whole blood viscosity. Hemodialysis International 16(3):342–350

Van Canneyt K, Pourchez T, Eloot S, Guillame C, Bonnet A, Segers P, Verdonck P (2010) Hemodynamic impact of anastomosis size and angle in side-to-end arteriovenous fistulae: a computer analysis. Journal of Vascular Access 11(1):52–58

Vignon-Clementel IE, Figueroa CA, Jansen KE, Taylor CA (2006) Outflow boundary conditions for three-dimensional finite element modeling of blood flow and pressure in arteries. Computer methods in applied mechanics and engineering 195(29):3776–3796

Vignon-Clementel IE, Figueroa CA, Jansen KE, Taylor CA (2010) Outflow boundary conditions for 3D simulations of non-periodic blood flow and pressure fields in deformable arteries. Computer Methods in Biomechanics and Biomedical Engineering 13(5):625–640

Wick T (2013) Solving monolithic fluid-structure interaction problems in Arbitrary Lagrangian Eulerian coordinates with the deal.II library. Archive of Numerical Software 1(1):1–19

Wick T (2015) Modeling, discretization, optimization, and simulation of fluid-structure interaction. Lecture notes, URL http://www.sciencedirect.com/science/article/pii/B9781856176354000145

Zhuang YJ, Singh T, Zarins C, Masuda H (1998) Sequential increases and decreases in blood flow stimulates progressive intimal thickening. European Journal of Vascular and Endovascular Surgery 16(4):301–310

Appendix 1

Linearized Navier–Stokes equations

Three directional derivatives of the momentum balance equation of the fluid in the reference configuration are required. The directional derivative with respect to a incremental velocity field $\Delta\mathbf{v}$ is given by

$$\begin{aligned} D_{\Delta v}(R_{\mathrm{f}},\delta\mathbf{v}) = &\int_{\Omega_{\mathrm{f}}} \delta\mathbf{v}\cdot J\rho_{\mathrm{f}}\frac{\partial\Delta\mathbf{v}}{\partial t}\mathrm{dV} \\ &+\int_{\Omega_{\mathrm{f}}} \delta\mathbf{v}\cdot J\rho_{\mathrm{f}}\,\mathrm{Grad}\,(\Delta\mathbf{v})\mathbf{F}^{-1}\mathbf{v}\,\mathrm{dV} \\ &+\int_{\Omega_{\mathrm{f}}} \delta\mathbf{v}\cdot J\rho_{\mathrm{f}}\mathrm{Grad}\,\mathbf{v}\mathbf{F}^{-1}\Delta\mathbf{v}\,\mathrm{dV} \\ &+\int_{\Omega_{\mathrm{f}}} \nabla\delta\mathbf{v} : J\rho_{\mathrm{f}}\nu_{\mathrm{f}}\,(\mathrm{Grad}\,(\Delta\mathbf{v})\mathbf{F}^{-1} \\ &\qquad +\mathbf{F}^{-T}\mathrm{Grad}(\Delta\mathbf{v})^{\mathrm{T}})\mathbf{F}^{-\mathrm{T}}\,\mathrm{dV}. \end{aligned} \tag{41}$$

Next the directional derivative resulting from a incremental displacement field in the mesh motion $\Delta\mathbf{u}$ is

$$\begin{aligned} D_{\Delta u}(R_{\mathrm{f}},\delta\mathbf{v}) = &\int_{\Omega_{\mathrm{f}}} \delta\mathbf{v}\cdot D_{\Delta u}(J)\rho_{\mathrm{f}}\Big(\Delta\mathbf{v}-\mathrm{Grad}\,\mathbf{v}\mathrm{f}\frac{\partial\mathbf{u}_{\mathrm{f}}}{\partial\mathrm{t}}\Big)\,\mathrm{dV} \\ &-\int_{\Omega_{\mathrm{f}}} \delta\mathbf{v}\cdot J\rho_{\mathrm{f}}\,\mathrm{Grad}\,\mathbf{v}\mathrm{D}_{\Delta u}\mathbf{F}^{-1}\frac{\partial\mathbf{u}_{\mathrm{f}}}{\partial\mathrm{t}}\,\mathrm{dV} \\ &-\int_{\Omega_{\mathrm{f}}} \delta\mathbf{v}\cdot J\rho_{\mathrm{f}}\,\mathrm{Grad}\,\mathbf{v}\mathbf{F}^{-1}\frac{\partial\Delta\mathbf{u}_{\mathrm{f}}}{\partial\mathrm{t}}\,\mathrm{dV} \\ &+\int_{\Omega_{\mathrm{f}}} \nabla\delta\mathbf{v} : D_{\Delta u}(J)\sigma_{\mathrm{f}}\mathbf{F}^{-T}\,\mathrm{dV} \\ &+\int_{\Omega_{\mathrm{f}}} \nabla\delta\mathbf{v} : J\sigma_f D_{\Delta u}\mathbf{F}^{-T}\,\mathrm{dV} \\ &+\int_{\Omega_{\mathrm{f}}} \nabla\delta\mathbf{v} : J\rho_{\mathrm{f}}\nu_{\mathrm{f}}\,(\mathrm{Grad}\,\mathbf{v}\mathrm{D}_{\Delta u}\mathbf{F}^{-1} \\ &\qquad +D_{\Delta u}\mathbf{F}^{-T}\,\mathrm{Grad}\,\mathbf{v}^{\mathrm{T}})\mathbf{F}^{-\mathrm{T}}\,\mathrm{dV}, \end{aligned} \tag{42}$$

with

$$\begin{aligned} D_{\Delta u}(J) &= \frac{\partial J}{\partial\mathbf{F}} : \nabla(\Delta\mathbf{u}) \\ &= J\mathbf{F}^{-1} : \nabla(\Delta\mathbf{u}) \\ &= J\mathbf{I} : \mathbf{F}^{-1}\nabla(\Delta\mathbf{u}), \end{aligned} \tag{43}$$

$$\begin{aligned} D_{\Delta u}(F^{-1}) &= \frac{\partial(\mathbf{F})}{\partial\mathbf{F}} : \nabla(\Delta\mathbf{u}) \\ &= -\mathbf{F}^{-1}\nabla(\Delta\mathbf{u})\mathbf{F}^{-1}, \end{aligned} \tag{44}$$

and

$$\begin{aligned} D_{\Delta u}(\mathbf{F}^{-T}) &= \frac{\partial(\mathbf{F}^{-T})}{\partial\mathbf{F}} : \nabla(\Delta\mathbf{u}) \\ &= -\mathbf{F}^{-T}\nabla(\Delta\mathbf{u})^{T}\mathbf{F}^{-T}. \end{aligned} \tag{45}$$

Lastly the directional derivative of the momentum equation with respect to an incremental change in the pressure field Δp is shown:

$$D_{\Delta p}(R_{\mathrm{f}}, \delta\mathbf{v}) = \int_{\Omega_{\mathrm{f}}} \nabla^{\mathbf{v}} : J\rho_{\mathrm{f}} \nu_{\mathrm{f}} \Delta p \mathbf{F}^{-T} \,\mathrm{dV}. \tag{46}$$

Directional derivatives for the incompressibility constraint are found with respect to the incremental changes in the velocity and displacement fields. Note that the directional derivative with respect to pressure is zero in the fluid domain. This results in zeroes on the diagonal of the Jacobian matrix on the fluid domain. The directional derivative for the incompressibility constraint with respect to Δv is given by

$$D_{\Delta v}(R_{\mathrm{f}}, \delta p) = \int_{\Omega_{\mathrm{f}}} \delta p\big(\mathrm{Div}\left(J\mathbf{F}^{-1}\Delta\mathbf{v}\right), \delta p\big)\,\mathrm{dV}, \tag{47}$$

and with respect to Δu by

$$\begin{aligned} D_{\Delta u}(R_{\mathrm{f}}, \delta p) = &\int_{\Omega_{\mathrm{f}}} \delta p\Big(\mathrm{Div}\left(\mathrm{D}_{\Delta u}(\mathrm{J})F^{-1}\mathbf{v}\right)\Big)\,\mathrm{dV} \\ &+ \int_{\Omega_{\mathrm{f}}} \delta p\Big(\mathrm{Div}\left(\mathrm{JD}_{\Delta u}(F^{-1})\mathbf{v}\right)\Big)\,\mathrm{dV}. \end{aligned} \tag{48}$$

Linearized mesh motion equations

The mesh motion equation is only a function of $\mathbf{u}$ and there is only one non–zero directional derivative:

$$D_{\Delta u}(R_{\mathrm{f}}, \delta\mathbf{u}) = \int_{\Omega_{\mathrm{f}}} \nabla\delta\mathbf{u} : \alpha\nabla(\Delta\mathbf{u})\,\mathrm{dV}. \tag{49}$$

Linearized structure equations

The linearized equations associated with the structure are as follows. The directional derivatives for $(25)_1$ are

$$D_{\Delta v}(R_{\mathrm{s}}, \delta\mathbf{v}) = \int_{\Omega_{\mathrm{s}}} \delta\mathbf{v} \cdot \rho_{\mathrm{s}} \frac{\partial\Delta\mathbf{v}}{\partial t}\,\mathrm{dV}, \tag{50}$$

$$D_{\Delta u}(R_{\mathrm{s}}, \delta\mathbf{v}) = \int_{\Omega_{\mathrm{s}}} \nabla\delta\mathbf{v} \cdot \big(\frac{\partial\mathbf{P}}{\partial\mathbf{F}} : \nabla(\Delta\mathbf{u})\big)\,\mathrm{dV}, \tag{51}$$

$$D_{\Delta p}(R_{\mathrm{s}}, \delta\mathbf{v}) = \int_{\Omega_{\mathrm{s}}} \nabla\delta\mathbf{v} \cdot \Delta p J\mathbf{F}^{-T}\,\mathrm{dV}. \tag{52}$$

The directional derivatives for $(25)_2$ are

$$D_{\Delta v}(R_{\mathrm{s}}, \delta\mathbf{u}) = -\int_{\Omega_{\mathrm{s}}} \delta\mathbf{u} \cdot \Delta\mathbf{v}\,\mathrm{dV}, \tag{53}$$

$$D_{\Delta u}(R_{\mathrm{s}}, \delta\mathbf{u}) = \int_{\Omega_{s}} \delta\mathbf{u} \cdot \rho_{\mathrm{s}}\Delta\mathbf{u}\,\mathrm{dV}. \tag{54}$$

The directional derivatives for $(25)_3$ are

$$D_{\Delta u}(R_{\mathrm{s}}, \delta p) = \int_{\Omega_{s}} \delta p\big(D_{\Delta u}(J)\big)\,\mathrm{dV}. \tag{55}$$

The tangent $\mathscr{A} = \partial\mathbf{P}/\partial\mathbf{F}$ can be split additively into an isotropic part and a part associated with anisotropic deformations,

$$\mathscr{A} = \mathscr{A}_{\mathrm{g}} + \mathscr{A}_{\mathrm{fib}}. \tag{56}$$

The calculations for the tangent make use of the chain rule. Before the tangent is computed, partial derivatives of (20) and the Cauchy–Green tensor are shown:

$$\begin{aligned} \Big[\frac{\partial S_{\mathrm{g}}}{\partial C}\Big]_{mjop} =&\mu\frac{\partial J^{-\frac{2}{3}}}{\partial C_{op}} I_{mj} - \big(\frac{\mu I_1}{3}\frac{\partial J^{-\frac{2}{3}}}{\partial C_{op}}\big)C^{-1}_{mj} \\ &- \big(\frac{\mu J^{-\frac{2}{3}}}{3}\frac{\partial I_1}{\partial C_{op}}\big)C^{-1}_{mj} - \big(\frac{\mu J^{-\frac{2}{3}} I_1}{3}\big)\frac{\partial C^{-1}_{mj}}{\partial C_{op}} \\ &+ p\big(\frac{\partial J}{\partial C_{op}}C^{-1}_{mj} + J\frac{\partial C^{-1}_{mj}}{\partial C_{op}}\big) \\ =&-\frac{1}{3}\mu J^{-\frac{2}{3}} I_{mj} C^{-1}_{op} + \\ &\big(pJC^{-1}_{op} - \frac{\mu}{3}\big(J^{-\frac{2}{3}} I_{op} - \frac{I_1}{3}J^{-\frac{2}{3}}C^{-1}_{op}\big)\big)C^{-1}_{mj} \\ &+ \frac{1}{2}\big(-pJ + \frac{\mu J^{-\frac{2}{3}} I_1}{3}\big)\big(C^{-1}_{mo}C^{-1}_{jp} + C^{-1}_{mp}C^{-1}_{jo}\big), \end{aligned} \tag{57}$$

and

$$\begin{aligned} \Big[\frac{\partial C}{\partial F}\Big]_{ijkl} &= \frac{[\partial F^T F]_{ij}}{\partial F_{kl}} = \frac{\partial(F^T_{im}F_{mj})}{\partial F_{kl}} \\ &= \frac{\partial F_{mi}}{\partial F_{kl}}F_{mj} + F_{mi}\frac{\partial F_{mj}}{\partial F_{kl}} \\ &= \delta_{mk}\delta_{il}F_{mj} + F_{mi}\delta_{mk}\delta_{jl} \\ &= \delta_{il}F_{kj} + F_{ki}\delta_{jl}. \end{aligned} \tag{58}$$

Using (57-58) the tangent associated with the ground matrix is calculated as

$$\begin{aligned}
\mathscr{A}_{\mathrm{g},ijkl} &= \Big[\tfrac{\partial \mathbf{P}}{\partial \mathbf{F}}\Big]_{ijkl} \\
&= \frac{\partial (F_{im}S_{mj})}{\partial F_{kl}} \\
&= \frac{\partial F_{im}}{\partial F_{kl}} S_{mj} + F_{im}\frac{\partial S_{mj}}{\partial C_{op}}\frac{\partial C_{op}}{\partial F_{kl}} \\
&= \delta_{ik}\delta_{ml}\Big(\mu J^{-\frac{2}{3}} I + \big(pJ - \frac{\mu J^{-\frac{2}{3}} I_1}{3}\big) C^{-1}\Big)_{mj} \\
&\quad + F_{im}\Big[\big(pJC^{-1}_{op} - \frac{\mu}{3}\big(J^{-\frac{2}{3}} I_{op} - \frac{I_1}{3} J^{-\frac{2}{3}} C^{-1}_{op}\big)\big) C^{-1}_{mj} \\
&\quad - \frac{1}{2}\big(pJ - \frac{\mu J^{-\frac{2}{3}} I_1}{3}\big)\big(C^{-1}_{mo}C^{-1}_{jp} + C^{-1}_{mp}C^{-1}_{jo}\big)\Big]\big(\delta_{ol}F_{kp} + F_{ko}\delta_{pl}\big) \\
&\quad + F_{im}\big[-\frac{1}{3}\mu J^{-\frac{2}{3}} C^{-1}_{op} I_{mj}\big]\big(\delta_{ol}F_{kp} + F_{ko}\delta_{pl}\big) \\
&= \delta_{ik}(\mu J^{-\frac{2}{3}} I_{lj} + \Big(pJ - \frac{\mu J^{-\frac{2}{3}} I_1}{3}\Big) C^{-1}_{lj}) \\
&\quad + F_{im}\Big[\big(pJC^{-1}_{lp} - \frac{\mu}{3}\big(J^{-\frac{2}{3}} I_{lp} - \frac{I_1}{3} J^{-\frac{2}{3}} C^{-1}_{lp}\big)\big) C^{-1}_{mj} \\
&\quad + \frac{1}{2}\big(-pJ + \frac{\mu J^{-\frac{2}{3}} I_1}{3}\big)\big(C^{-1}_{ml}C^{-1}_{jp} + C^{-1}_{mp}C^{-1}_{jl}\big)\Big] F_{kp} \\
&\quad + F_{im}\Big[\Big(pJC^{-1}_{ol} - \frac{\mu}{3}\big(J^{-\frac{2}{3}} I_{ol} - \frac{I_1}{3} J^{-\frac{2}{3}} C^{-1}_{ol}\big)\Big) C^{-1}_{mj} \\
&\quad + \frac{1}{2}\big(-pJ + \frac{\mu J^{-\frac{2}{3}} I_1}{3}\big)\big(C^{-1}_{mo}C^{-1}_{jl} + C^{-1}_{ml}C^{-1}_{jo}\big)\Big] F_{ko} \\
&\quad + F_{im}\Big[-\frac{1}{3}\mu J^{-\frac{2}{3}} C^{-1}_{lp} I_{mj}\Big] F_{kp} + F_{im}\Big[-\frac{1}{3}\mu J^{-\frac{2}{3}} C^{-1}_{ol} I_{mj}\Big] F_{ko}.
\end{aligned}$$

The tangent associated with the fibres can be calculated using (23),(24) and (58) as:

$$\begin{aligned}
\mathscr{A}_{\mathrm{fib},ijkl} &= \Big[\tfrac{\partial \mathbf{P}}{\partial \mathbf{F}}\Big]_{ijkl} \\
&= \frac{\partial (F_{im}S_{mj})}{\partial F_{kl}} \\
&= \frac{\partial F_{im}}{\partial F_{kl}} S_{\mathrm{fib},mj} + F_{im}\frac{\partial S_{\mathrm{fib},mj}}{\partial C_{op}}\frac{\partial C_{op}}{\partial F_{kl}} \\
&= \Big[\delta_{ik}S_{\mathrm{fib,lj}} \\
&\quad + F_{im}\Big[\frac{\partial S_{\mathrm{fib}}}{\partial C}\Big]_{mjop}\big(\delta_{ol}F_{kp} + F_{ko}\delta_{pl}\big)\Big] \\
&= \Big[\delta_{ik}\big[(2k_1G_i)\exp\big(k_2G_i^2\big)\frac{\partial G_i}{\partial C}\big]_{lj} \\
&\quad + F_{im}\big(2\frac{\partial S_{f,mj}}{\partial I_1}F_{ko}I_{ol} + \frac{\partial S_{f,mj}}{\partial I_4}F_{kp}A^T_{pl} \\
&\quad + \frac{\partial S_{f,mj}}{\partial I_4}F_{ko}A_{ol}\big)\Big],
\end{aligned} \tag{59}$$

with

$$\begin{aligned}
\Big[\frac{\partial S_{\mathrm{fib}}}{\partial C}\Big]_{mjop} &= \frac{\partial S_{\mathrm{fib},mj}}{\partial I_1}\frac{\partial I_1}{\partial C_{op}} + \frac{\partial S_{\mathrm{fib},mj}}{\partial I_i}\frac{\partial I_i}{\partial C_{op}} \qquad (60) \\
\frac{\partial S_{\mathrm{fib},mj}}{\partial I_1}\frac{\partial I_1}{\partial C_{op}} &= 2k_1\Big[\frac{\partial G}{\partial I_1}\exp\big(k_2G_i^2\big)\frac{\partial G_i}{\partial C} \\
&\quad + G\frac{\partial\Big(\exp\big(k_2G_i^2\big)\Big)}{\partial I_1}\frac{\partial G_i}{\partial C} \\
&\quad + G\exp\big(k_2G_i^2\big)\frac{\partial}{\partial I_1}\big(\frac{\partial G_i}{\partial C}\big)\Big]_{mj} I_{op} \\
&= 2k_1\Big[\kappa J^{-\frac{2}{3}}\exp\big(k_2G_i^2\big)\frac{\partial G_i}{\partial C} \\
&\quad + 2k_2\kappa G^2 J^{-\frac{2}{3}}\exp\big(k_2G_i^2\big)\frac{\partial G_i}{\partial C} \\
&\quad + \frac{1}{3}\kappa J^{-\frac{2}{3}} G\exp\big(k_2G_i^2\big)C^{-1}\Big]_{mj} I_{op} \qquad (61) \\
\frac{\partial S_{\mathrm{fib},mj}}{\partial I_i}\frac{\partial I_i}{\partial C_{op}} &= 2k_1\Big[\frac{\partial G}{\partial I_i}\exp\big(k_2G_i^2\big)\frac{\partial G_i}{\partial C} \\
&\quad + G\frac{\partial(\exp\big(k_2G_i^2\big))}{\partial I_i}\frac{\partial G_i}{\partial C} \\
&\quad + G\exp\big(k_2G_i^2\big)\frac{\partial}{\partial I_i}\big(\frac{\partial G_i}{\partial C}\big)\Big]_{mj} A_{op} \\
&= 2k_1\Big[(1-3\kappa)J^{-\frac{2}{3}}\exp\big(k_2G_i^2\big)\frac{\partial G_i}{\partial C} \\
&\quad + 2k_2G^2(1-3\kappa)J^{-\frac{2}{3}}\exp\big(k_2G_i^2\big)\frac{\partial G_i}{\partial C} \\
&\quad + \frac{1}{3}(1-3\kappa)J^{-\frac{2}{3}} G\exp\big(k_2G_i^2\big)C^{-1}\Big]_{mj} A_{op}.
\end{aligned} \tag{62}$$

Appendix 2

Linearization of backflow stabilization

The linearization of the boundary condition as requires a precomputed global vector which contains the linearization of the flow terms

$$D_{\Delta\mathbf{v}}Q_{\mathrm{out}} = \int_{\Gamma_{\mathrm{out}}} \Delta\mathbf{v}\cdot J\mathbf{F}^{-T}\mathbf{N}\,\mathrm{dS}. \tag{63}$$

$D_{\Delta\mathbf{v}}Q_{\mathrm{out}}$ is the directional derivative of Q_{out} at a given velocity $\mathbf{v}$ in the direction of the incremental velocity field $\Delta\mathbf{v}$. The linearization of the second term in (30) using the generalized resistive boundary condition is given by

$$D_{\Delta v}f(Q_{\mathrm{out}}) = \Big(\int_{\Gamma_{\mathrm{out}}} \delta\mathbf{v}\cdot J\mathbf{F}^{-T}\mathbf{N}\,\mathrm{dS}\Big)\big(f'(\mathrm{Q_{out}})\big)\mathrm{D}_{\Delta v}\mathrm{Q_{out}}. \tag{64}$$

For the particular case of a purely resistive boundary, such as present in (30), $f(Q_{\mathrm{out}}) = R_R Q_{\mathrm{out}}$ and the derivative to be used in (64) is $f'(Q_{\mathrm{out}})) = R_R$.

Appendix 3

Weak form of Windkessel model

To prescribe the relationship between the flow and pressure, $f(Q_{\text{out}})$ is given by

$$f(Q_{\text{out}}) = R_R \int_{\Gamma_{\text{out}}} \mathbf{v} \cdot J\mathbf{F}^{-T}\mathbf{N}\,\mathrm{dS} + \int_0^{\mathrm{t_{n+1-\alpha_f}}} \frac{\mathrm{e}^{-\frac{\mathrm{t-s}}{\tau}}}{\mathrm{C}}\mathrm{Q_{out}}\,\mathrm{ds} \tag{65}$$

where C is the capacitance, R_R the resistance at the outlet, $\tau = R_{\mathrm{d}}C$ the relaxation parameter, and R_d the resistance downstream. The velocity evaluated at some time s during the timestep t^l to t^{l+1} is given by

$$\begin{aligned}\mathbf{v}(s) &= \mathbf{v}^l + (\mathbf{v}^{l+1} - \mathbf{v}^l)\big(\frac{s-t_l}{t_{l+1}-t_l}\big) \\ &= \mathbf{v}^l\big(\frac{t_{l+1}-s}{\triangle t}\big) + \mathbf{v}^{l+1}\big(\frac{s-t_l}{\triangle t}\big).\end{aligned} \tag{66}$$

Here $\triangle t$ is the size of the timestep. After time discretization $f(Q_{\text{out}}^{n+1-\alpha_{\mathrm{f}}})$ can be evaluated by

$$f(Q_{\text{out}}^{n+1-\alpha_f}) = R_R\big((1-\alpha_{\mathrm{f}})Q^{n+1} + \alpha_{\mathrm{f}}Q^n\big) + h^{n+1}, \tag{67}$$

where h^{n+1} is given by

$$\begin{aligned}h^{n+1} = \big(e^{-\frac{\triangle t}{\tau}}\big)h^n + \int_{t_n}^{t_{n+1-\alpha_{\mathrm{f}}}} \frac{e^{-\frac{t-s}{\tau}}}{C}\Big(Q_{\text{out}}^n\big(\frac{t_{n+1}-s}{\triangle t}\big) \\ + Q_{\text{out}}^{n+1}\big(\frac{s-t_n}{\triangle t}\big)\Big)\,\mathrm{ds}.\end{aligned} \tag{68}$$

Finally, after integrating over time,

$$\begin{aligned}h^{n+1} =& \big(e^{-\frac{\triangle t}{\tau}}\big)h^n \\ &+ R_d\Big[Q^n\Big(\frac{t_{n+1}-t_{n+1-\alpha_{\mathrm{f}}}}{\triangle t} - e^{-\frac{t-s}{\tau}} + \frac{\tau}{\triangle t}\big(1-e^{-\frac{t-s}{\tau}}\big)\Big) \\ &+ Q^{n+1}\Big(\frac{t_{n+1-\alpha_{\mathrm{f}}}-t_n}{\triangle t} - \frac{\tau}{\triangle t}\big(1-e^{-\frac{t-s}{\tau}}\big)\Big)\Big].\end{aligned} \tag{69}$$